JGR Oceans

RESEARCH ARTICLE
10.1029/2019JC015704

Monitoring Intense Oceanic Fronts Using Sea Surface Roughness: Satellite, Airplane, and In Situ Comparison

Nicolas Rascle[1,2], Bertrand Chapron[2], Jeroen Molemaker[2,3], Frédéric Nouguier[2], Francisco J. Ocampo-Torres[1], J. Pedro Osuna Cañedo[1], Louis Marié[2], Björn Lund[4], and Jochen Horstmann[5]

[1]Departamento de Oceanografía Física, Centro de Investigación Científica y de Educación Superior de Ensenada, Ensenada, México, [2]Université de Bretagne Occidentale, CNRS, IRD, Ifremer, Laboratoire d'Océanographie Physique et Spatiale (LOPS), IUEM, Brest, France, [3]Department of Atmospheric and Oceanic Sciences, University of California Los Angeles, Los Angeles, CA, USA, [4]Department of Ocean Sciences, Rosenstiel School of Marine and Atmospheric Science, University of Miami, Miami, FL, USA, [5]Department of Radar Hydrography, Helmholtz-Zentrum Geesthacht, Geesthacht, Germany

Key Points:
- Sea surface roughness induced by a submesoscale oceanic front is measured from satellite and airplane during a drifter release experiment
- Drifters unambiguously show extreme frontal sharpness with extreme current gradients, including both convergence and cyclonic vorticity
- Accurate monitoring of such sharp front using surface roughness is demonstrated and hinges on the availability of high-resolution sensors

Supporting Information:
- Supporting Information S1
- Movie S1
- Movie S2
- Movie S3
- Movie S4

Correspondence to:
N. Rascle,
nrascle@cicese.mx

Citation:
Rascle, N., Chapron, B., Molemaker, J., Nouguier, F., Ocampo-Torres, F. J., & Osuna Cañedo, J. P., et al. (2020). Monitoring intense oceanic fronts using sea surface roughness: Satellite, airplane, and in situ comparison. *Journal of Geophysical Research: Oceans*, *125*, e2019JC015704. https://doi.org/10.1029/2019JC015704

Received 1 OCT 2019
Accepted 27 JUN 2020
Accepted article online 3 JUL 2020

Abstract Sea surface roughness is affected by surface current gradients, which provides a means of monitoring from satellite sharp oceanic fronts. This paper is the second report of an experiment designed to compare observations of sea surface roughness and surface currents at an unprecedented accuracy, owing to the conjunction of numerous deployed drifters and roughness instruments. About 200 drifters sampled a thin 10 km elongated submesoscale front, also monitored by a high density of roughness instruments: satellite synthetic aperture radar, satellite, and airborne multiangle sunglint radiometers. The first paper focused on the retrieval of the current gradient direction (convergence and cyclonic vorticity) at the front, using roughness observations at multiple angle from airplane. This second paper focuses on the retrieval of the current gradient magnitude and scale, using roughness observations at different scales, from airplane and from satellite. Two main results are obtained: (i) Trajectories of selected drifters show that the front is only 50 m wide and unambiguously exhibits convergence and cyclonic vorticity up to 100f (with f the Coriolis frequency). This far exceeds previously documented values for submesoscale deep ocean fronts. (ii) Correct estimation of such extreme current gradients using surface roughness hinges on instruments with sufficiently high spatial resolution. Lower-resolution roughness sensors can still detect the front, as demonstrated from observations and a simplified model, but cannot properly estimate the current gradient magnitude and the frontal width. Those results provide guidelines for monitoring intense current gradients from space using sea surface roughness.

Plain Language Summary Ocean surface currents are not uniform horizontally but involve structures of many different sizes. After focusing on large-scale currents (about 1,000 km) and eddies (about 100 km), attention is nowadays turning toward fine-scale (about 1 km) fronts and filaments. Those fine structures are indeed particularly important for the exchanges between ocean surface and deeper ocean, for the accumulation of drifting pollution, and for the concentration of biological production and marine predators. Fishermen well know that oceanic fronts can be revealed by visual inspection of the ocean surface roughness. Exploring this idea, this paper investigates how oceanic fronts can be monitored using images of sea surface roughness. Images from satellites and airplanes were taken during an experiment where hundreds of surface drifters were released and got caught within an intense front. Two new lessons are learned from those observations: (1) The front was only 50 m wide, which is much sharper than commonly assumed for fronts of this type. (2) The front is thus associated with extreme current shear, which can only be detected by roughness sensors with sufficiently high spatial resolution. Those are important findings to improve monitoring of intense oceanic fronts from satellite.

1. Introduction

Fronts are ubiquitous features of the ocean surface, as often spectacularly revealed by high-resolution satellite images of sea surface temperature (SST), ocean color, or sea surface roughness. Those fronts commonly

sharpen to scales less than 10 km and can develop intense current gradients. In that respect they are oceanic analogs of atmospheric surface fronts. At those scales, the fronts escape the geostrophic dynamical balance of larger eddies, to develop large localized vertical velocities, stimulating exchanges between surface and deeper ocean (Klein & Lapeyre, 2009). Small-scale fronts can further concentrate surface drifting materials within thin convergence areas (D'Asaro et al., 2018). Fronts are thus hot spots for biology (Grimes & Finucane, 1991; Mahadevan, 2016; Woodson & Litvin, 2015) and for drifting pollution (Zhong et al., 2012), including plastics and *Sargassum*.

Monitoring those fronts from space is a challenge because very high resolution sensors are required. Infrared SST and visible ocean color images provide synoptic views at adequate resolution and have historically supported frontal studies (e.g., Fedorov, 1986; Simpson, 1981). Nonetheless, as noted by Mueller and LaViolette (1981), temperature and color contain incomplete (and at times complementary) information on the front dynamical activity, because temperature can be compensated by salinity (e.g., Ferrari & Rudnick, 2000; Jaeger & Mahadevan, 2018) and because ocean color is not a conservative tracer. On the contrary, sea surface roughness modulations are known direct evidence of surface current gradients at fronts. The main physical mechanism is refraction or modulation of short waves by surface currents (Phillips, 1984). [Note that there are other mechanisms than direct wave-current interaction, which can be responsible for surface roughness modulations around fronts. One is the presence of surfactants, which is mainly restricted to very low wind speed (Chust & Sagarminaga, 2007; Cooper et al., 2005; Kudryavtsev et al., 2012a; Matthews et al., 1997)]. Another one is wind modification around the front, which most likely occurs at larger horizontal scales (see discussion by Kudryavtsev et al., 2005), except around floating debris (Matthews et al., 2017). Thus, valuable information on surface currents can be obtained from sea surface roughness images (as, e.g., obtained by synthetic aperture radar [SAR] or by radiometers looking within the sunglint) to complement temperature and color observations.

Quantifying surface current gradients from surface roughness observations has been attempted since the first observations became available (e.g., Alpers, 1985; Apel et al., 1975; Jackson et al., 2013; Jansen et al., 1998; Johannessen et al., 2005; Marmorino et al., 1999). The consensus at present is that surface current refracts and impacts waves of intermediate scales (wavelength of 1 to 10 m), modulating breaking and near-breaking waves, which in turn modulate roughness scatters sensed by radars or radiometers (Kudryavtsev et al., 2005; Lyzenga, 1998; Thompson & Gasparovic, 1986). The current gradient around a nearly infinite rectilinear front has two components, along front and across front ($\partial u/\partial x$ and $\partial v/\partial x$, using the notations of section 4), which can be described by a magnitude and a direction. Recent investigations have been devoted to retrieve the current gradient direction (Dulov & Kudryavtsev, 1990; Lyzenga, 1991) and demonstrated the need to observe the ocean front at multiple view angles (Rascle et al., 2014, 2016). This bears similarity with medium-resolution scatterometer roughness measurements, with necessary observations at different azimuth angles to retrieve both the wind speed and direction. Some high-resolution satellite radiometers possess this multiangle capability (e.g., ASTER, Matthews, 2005; PRISM, Matthews & Awaji, 2010; and Multiangle Imaging SpectroRadiometer (MISR), Chust & Sagarminaga, 2007), but the difference between the view angles is at present too large to confidently retrieve current gradient direction from the surface roughness anomaly (Rascle et al., 2018).

To advance further, an experiment was designed to compare surface roughness observations to surface currents at unprecedented resolution and accuracy, taking advantage of the deployment of large number (about 1,000) of drifters, in conjunction with numerous instruments measuring surface roughness (satellite SAR, satellite multiangle radiometer, and airplane multiangle radiometer). In a first paper (Rascle et al., 2017), a new method using roughness observations from airplane at multiple angles was detailed. From an airborne instrument, a dense distribution of view angles was obtained, which permitted to retrieve current gradient direction, namely, convergence plus cyclonic vorticity. Those observations also suggested very large current gradient magnitudes, which could not be validated at that time because of two difficulties. First, airplane observations could only cover horizontal scales less than 100 m (see section 2.3). Second, current velocities derived from statistics of drifter trajectories (e.g., Pearson et al., 2019) and X-band radars (Lund et al., 2018) did not offer sufficiently high spatial resolution.

The retrieval of the current gradient magnitude is the focus of this second paper. Airplane measurements are now combined with satellite measurements covering a different range of horizontal scales. We seek answers

to the following questions: Down to what horizontal scale can frontal current gradients sharpen? What is then the typical current gradient magnitude? Which roughness instrument is able to detect it and provide a correct estimation of its horizontal scale?

The experiment is described in section 2, with a general overview of the front, the drifters and the surface roughness observations. Then an estimation of the current gradient from in situ observations is done in section 3 and shows that the front was much sharper than any previously documented submesoscale front. The estimation of the current gradient from satellite and airplane surface roughness follows in section 4. The range of horizontal scales covered by the instruments is shown to be crucial. Finally, section 5 discusses some future strategies to monitor such intense fronts from space and gives some geophysical perspectives.

2. The Experiment

2.1. Overview

The experiment took place on January–February 2016 as part of LASER (LAgrangian Submesoscale ExpeRiment, Özgökmen et al., 2014). A very large number (about 1,000) of surface (at 0.6 m depth) drifters were deployed to study surface dispersion in the northern Gulf of Mexico, specifically targeting submesoscale oceanic features (D'Asaro et al., 2018). Two research vessels helped the deployment and gathered measurements, together with up to three different airplanes making surface measurements, with one specifically equipped to retrieve multiangle sunglint.

During the last days of the experiment, an elongated front developed along the continental shelf (Figure 1a) and began to interact with a rapidly spiraling eddy. This type of interaction is often observed at the ocean surface (e.g., Eldevik & Dysthe, 2002; Munk et al., 2000). The surface roughness image (Figure 1b) suggests that frontal currents were particularly intensified in two distinct regions, one northwest of the eddy center (black box in Figure 1b) and one southeast of the eddy center.

About 200 drifters got caught within the northwest part of the spiraling front, while the R/V Walton Smith sampled the front and redeployed drifters (see Movie S1 in the supporting information). More details of the oceanographic context of this front, including vertical hydrography and dynamics, can be found in D'Asaro et al. (2018).

2.2. Surface Roughness Instruments

Thanks to a coincidence of the orbits on 11 February 2016, the front was sampled by the SAR on board the satellite Sentinel-1a (Torres et al., 2012) at 11:50 UTC and then by MISR (Diner et al., 1989) on board the satellite Terra at 16:43 UTC. In addition, the airplane carrying a multiangle visible radiometer made six successive passes over the same front from 19:12 to 19:53 UTC. The drifters trajectories at 11:50, 16:43, and 19:26 UTC and the corresponding surface roughness images are shown in Figures 2a–2i with a frame size of about 25 km. The full temporal evolution of the drifters, together with the corresponding roughness images, can be better appreciated in Movie S1. A zoom over different parts of the front at those three different times is shown in Figure 3, with a frame size of about 4 km. Again, the temporal evolution can be appreciated in Movies S2 and S3.

Sentinel-1a acquired two C-band SAR images, in copolarization VV and cross-polarization VH, at about 41° incidence angle. Both images were taken in the Interferometric Wide (IW) mode, which has a nominal spatial resolution of about 20 m. MISR acquired nine images at different view angles between 16:40 and 16:46 UTC. The 672 nm radiance is used, with a spatial resolution about 275 m. More explanations on MISR sunglint geometry can be found in Rascle et al. (2018, their Figure 5a). The airplane acquired sequences of images at varying view angles (see Movie S4), out of which composites were created by restrictions to a given view angle range. For instance, the Composite C05 shown in Figure 3h was obtained using zenith angles lower than 10° and azimuth angles in the range [−22.5°, +22.5°]. More details on those airplane composites can be found in Rascle et al. (2017). The pixel ground resolution of the airplane measurement is about 5 m. The viewing geometry is shown in magenta in Figures 1–3 and in Movie S4.

In the remaining of the paper, surface roughness will refer to the normalized radar cross section (NRCS) σ in the case of SAR images and to the brightness intensity B in the case of sunglint images.

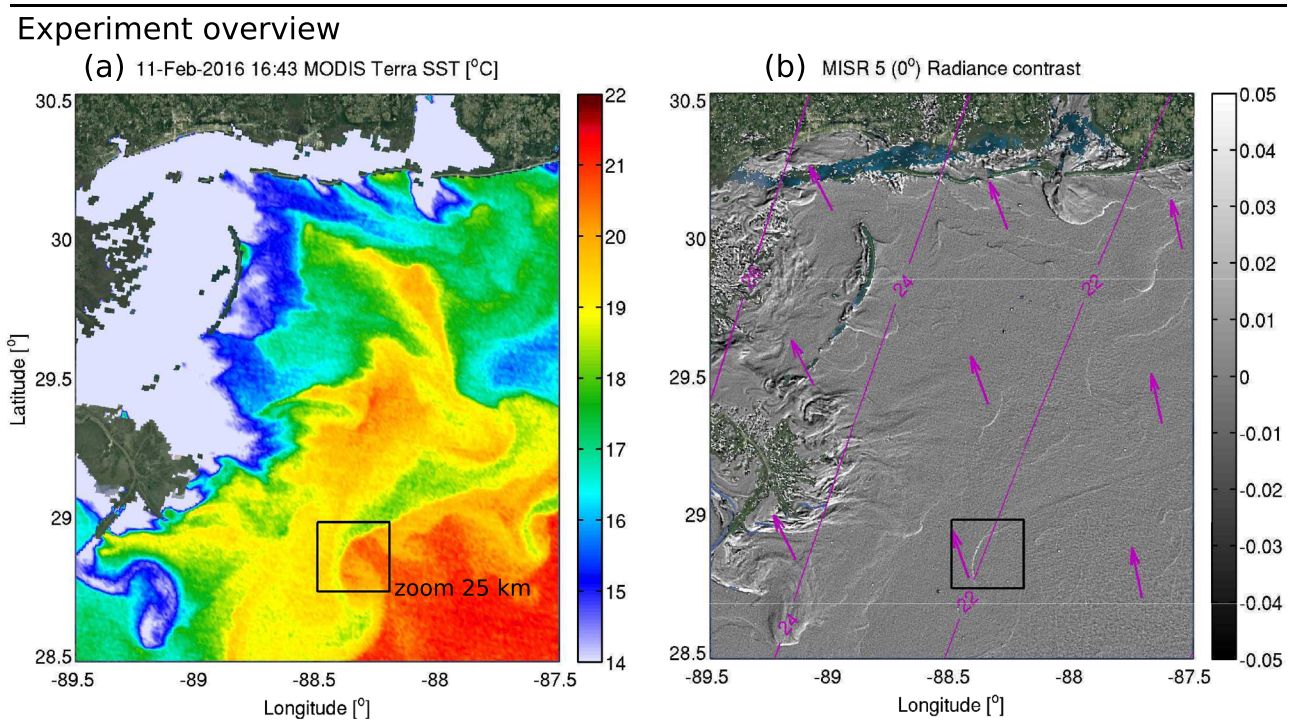

Figure 1. (a) Sea surface temperature from MODIS Terra and (b) sunglint radiance contrast from MISR Camera #5, on 11 February 2016 at 16:43 UTC. The black box shows the boundaries of the zoom at 25 km (shown in Figure 2). Magenta contours and arrows show, respectively, zenith and azimuth angles of the sunglint reflective facets.

2.3. Surface Roughness Contrast

The current gradient and the view geometry both affect the brightness intensity B of the sunglint image. Because geometry varies slowly across the image, its effect can be removed using a spatial high-pass filter with a cutoff scale L. We thus produce the image contrast B'/B, where B' is the high-pass-filtered brightness intensity. The cutoff scale L is chosen to be 10 km for the MISR polar-orbiting satellite. A similar treatment is applied to SAR Sentinel-1a data. For the airplane images, due to the low flying altitude (about 1,000 m), the cutoff scale has to be reduced to 100 m; otherwise, the sunglint geometry cannot be considered constant across the image. This is the strongest limitation of the airplane surface roughness measurements: They do not cover scales larger than 100 m.

Note that the cutoff scale could have been chosen even larger for the satellite images. However, the current gradient is not the only geophysical source of surface roughness variations, as variations of the wind field are also important. Filtering scales larger than 10 km removes most wind variations. Finer-scale wind variations remain apparent on the images (e.g., convective cells in Figure 2b and wind streaks in Figures 2e, 2f, 3h, and 3i) but have very distinctive spatial structures and we assume that they are not directly related to the front. In the vicinity of the front, we assume that direct surface current impact on waves is the dominant source of roughness variations (Kudryavtsev et al., 2005).

2.4. Observed Roughness Contrasts at the Front

There is a striking agreement between the location of the surface drifters and the location of the surface roughness contrasts. It demonstrates that the drifters or any similar buoyant material trapped into a convergence zone could be located by surface roughness observations at a spatial accuracy of about 500 m using MISR observations (Figures 2d–2f), about 100 m using SAR observations (Figures 3a and 3b), and about 50 m using airplane observations (Figures 3g–3i). This accuracy is illustrated at medium resolution in Movie S1 and at high resolution for each airplane pass in Movie S4.

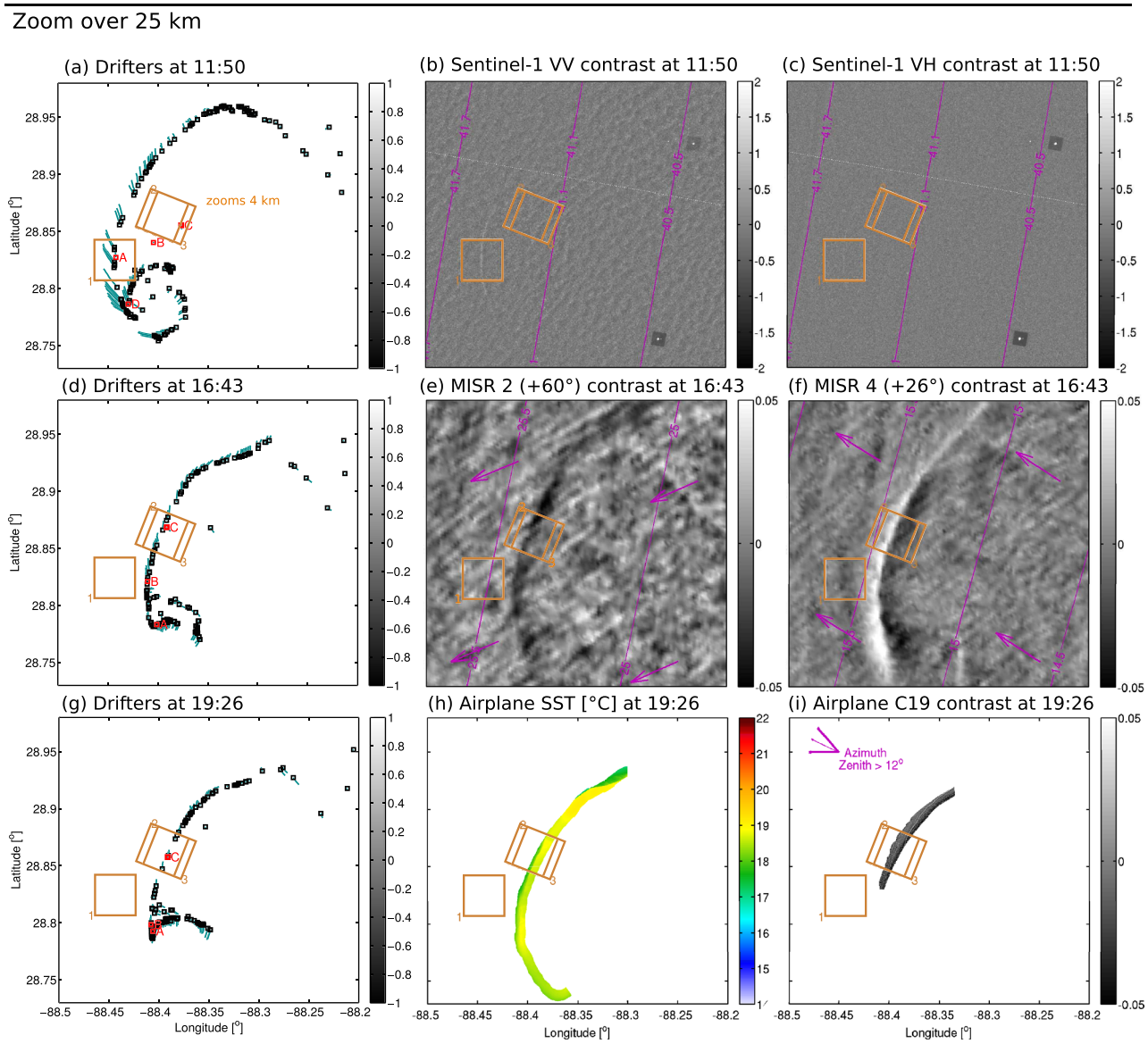

Figure 2. (a) Drifters positions and last hour trajectories on 11 February 2016 at 11:50UTC. (b, c) NRCS contrasts of Sentinel-1 SAR in VV and VH polarizations, respectively, at 11:50UTC. (d) Drifters at 16:43UTC. (e, f) Sunglint radiance contrasts of MISR Cameras #2 and #4, respectively, at 16:43UTC. (g) Drifters at 19:26 UTC. (h, i) SST and sunglint radiance contrast (Composite C19), respectively, measured from airplane at between 19:25 and 19:33UTC. The drifters (A, B, C, and D) used for gradient calculations are shown as red squares (Drifter D is only showed at 11:50 as it ends up very close to Drifter A at subsequent times). The three orange boxes (1, 2, and 3) are the boundaries of the three zooms at 4km shown in Figure 3. In (b) and (c) magenta contours show the (zenith) incidence angles. In (e) and (f) magenta contours and arrows show, respectively, zenith and azimuth angles of the sunglint reflective facets.

Each instrument shows a different surface roughness contrast at the front, with a different contrast sign, amplitude, spatial extension, and spatial resolution. Transects orthogonal to the front are shown in Figure 4a. Figure 5 shows more details over the front and summarizes the roughness frontal width (defined in the caption) and contrast observed by each instrument.

- The MISR observations, which cover spatial scales in the range [275m, 10km], show the largest frontal width, about 0.5 to 3km. The roughness contrast displays sign changes according to the viewing geometry between the different MISR cameras (Figures 2e and 2f), as discussed, for example, by McClain and Strong (1969), Jackson and Alpers (2010), Kudryavtsev et al. (2012a), and Rascle et al. (2018).
- The SAR observation in VV polarization, which covers scales in the range [20m, 10km], shows a sharper front than MISR, with frontal width about 100 to 300m. The inherent speckle noise limits the effective

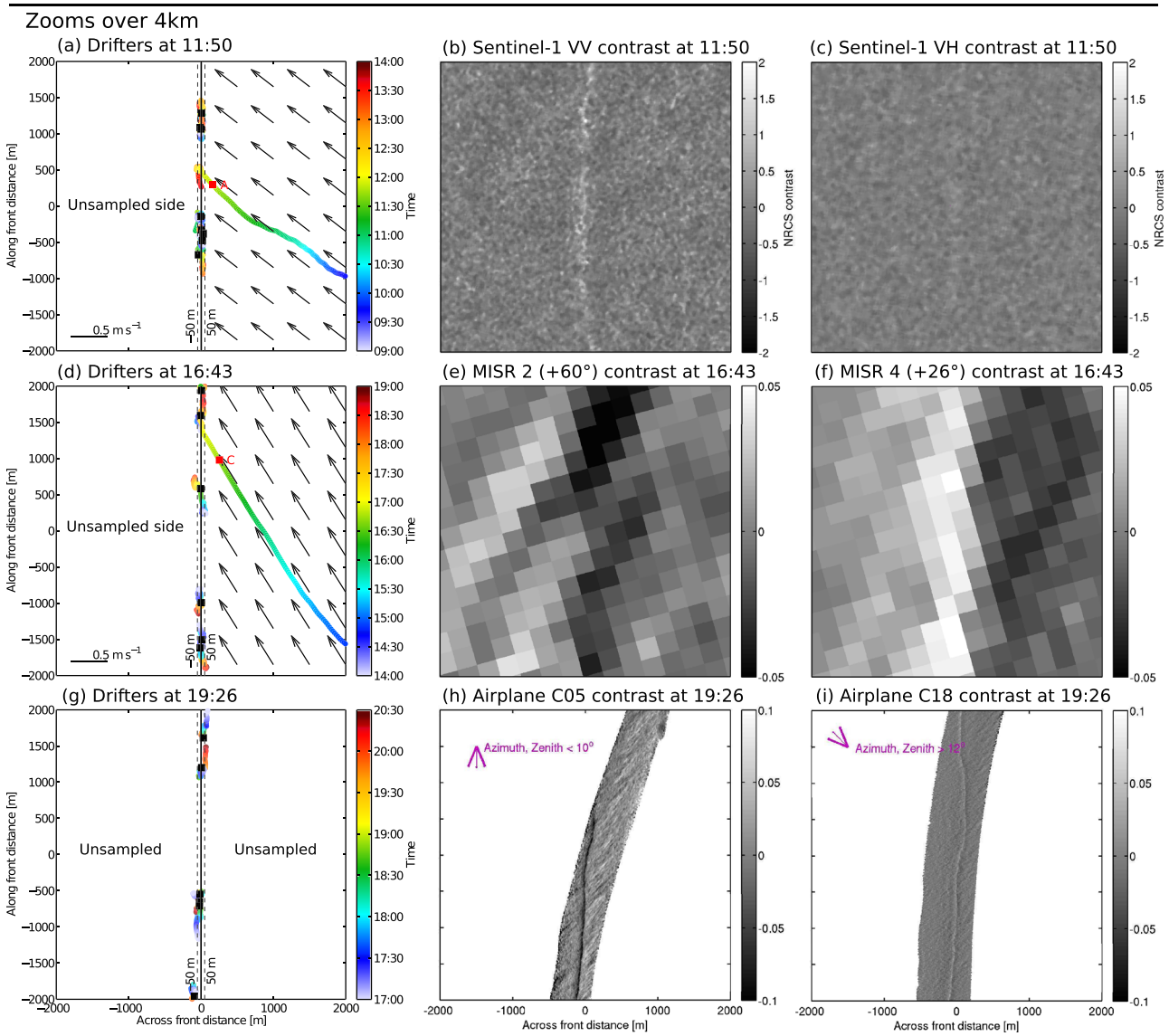

Figure 3. Zoom over the orange Frames #1 (top row), #2 (middle row), and #3 (bottom row) of the previous figure. (a) Drifters positions at 11:50UTC and trajectories from 9:30 to 14:00UTC, in the frame of reference of the front, defined by the 12 drifters in black around Drifter A in red. The black arrows show an estimated fit of Drifter A trajectory, namely, an along-front current of $0.24\,m\,s^{-1}$ plus an across-front current of $0.31\,m\,s^{-1}$. (b, c) NRCS contrasts of Sentinel-1 SAR in VV and VH polarizations, respectively, at 11:50UTC. (d) Same as (a) but at 16:43UTC and for eight drifters around Drifter C. The black arrows show an along-front current of $0.40\,m\,s^{-1}$ plus an across-front current of $0.25\,m\,s^{-1}$. (e, f) Sunglint radiance contrasts of MISR Cameras #2 and #4 at 16:43UTC. (g) Same as (d) but at 19:26UTC, when no drifter was available outside of the front. (h, i) Sunglint radiance contrast (Composites C05 and C18) from airplane cameras, using only a selection of zenith and azimuth angles (shown in magenta) of the sunglint reflective facets.

resolution of the instrument. The VH polarization exhibits a weak but detectable roughness contrast at the front. Its weakness was expected because the VH polarization has a weaker signal-to-noise ratio than VV polarization in moderate wind conditions (Kudryavtsev et al., 2014) and because noise level rises at those incidence angles (Mouche & Chapron, 2015). Nevertheless, the very weak roughness contrast observed in VH polarization likely informs about the modulation of surface wave breakers by the current variations. More specifically, copolarized VV radar returns are essentially enhanced with increasing numbers of steep and breaking quasi-specular scatters (Kudryavtsev et al., 2014). On the contrary, cross-polarized VH radar returns are not sensitive to quasi-specular scatters but to isotropic scatters generated during intense breaking wave crest events. Wave breaking modulations induced by

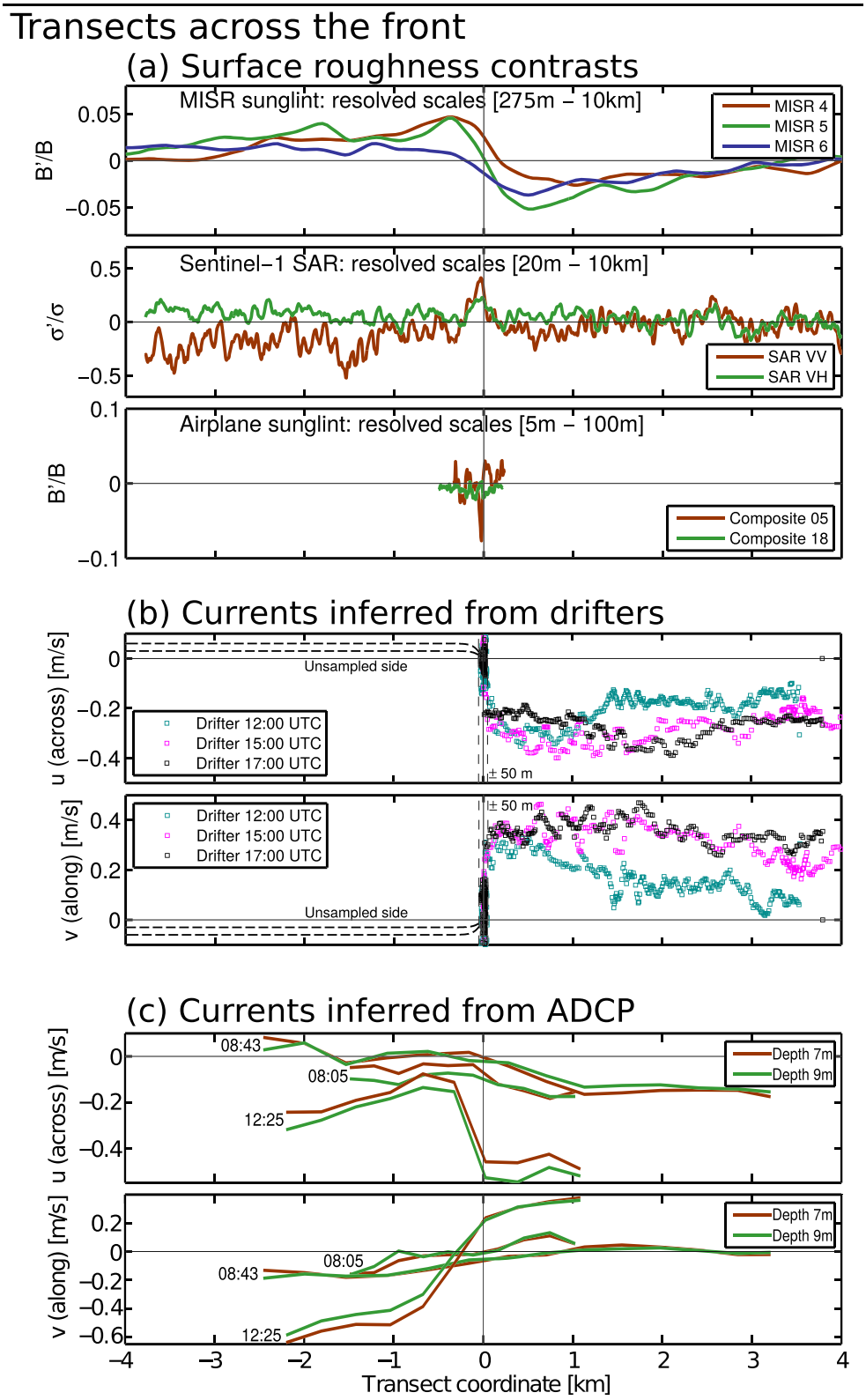

Figure 4. (a) Transects of the surface roughness contrasts within the front. (upper panel) MISR radiance contrast B'/B across orange Frame 2 at 16:43UTC. (middle panel) Sentinel-1 NRCS contrast σ'/σ across Frame 1 at 11:50UTC. (lower panel) Airplane radiance contrast B'/B across Frame 3 at 19:26UTC. (b) Currents inferred from trajectories of Drifters A (at 12:00UTC), B (at 15:00UTC), and C (at 17:00UTC). (c) Currents measured by ship ADCP during front crosses at 08:05, 08:43 and 12:25UTC. In (b) and (c), velocities are defined in local front-following frame of reference.

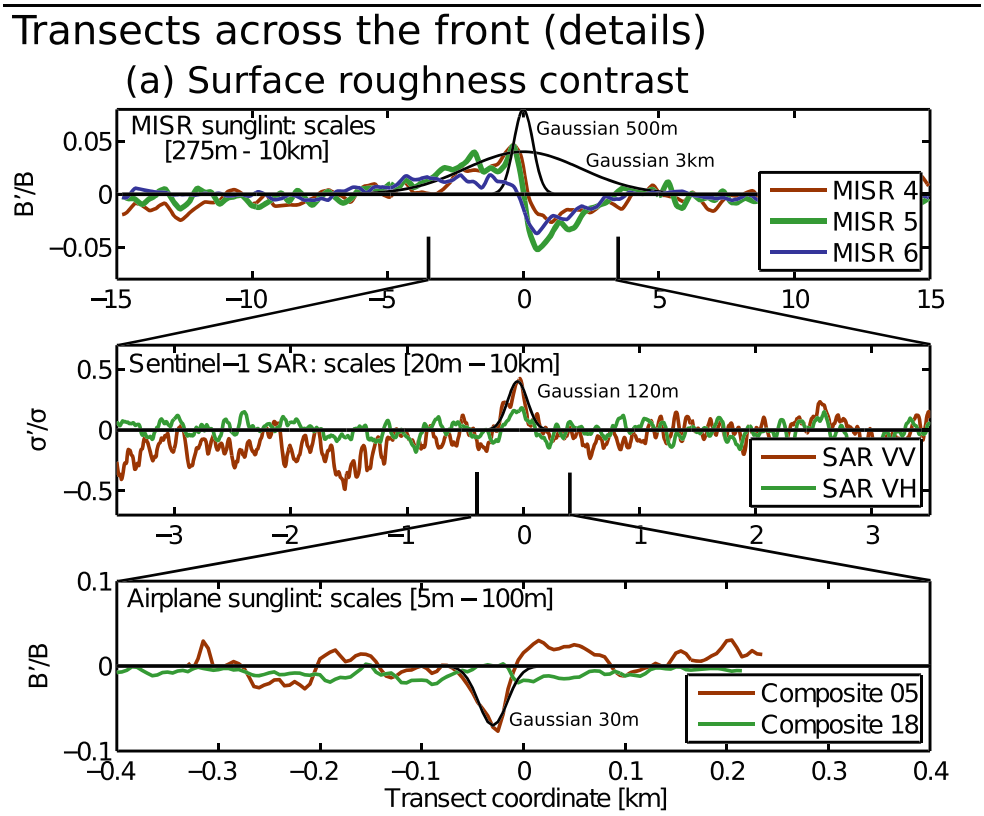

(b) Surface roughness contrast summary

Data	Observed scales	Frontal width			Contrast at scales [5m 100m]	Contrast at scales [275m 10km]
		80%	50%	20%		
MISR 4, 5, 6, 7	[275m 10km]	600 m	1200 m	3500 m	Undef	~5%
SAR VV	[20m 10km]	70 m	110 m	230 m	Noise	~5%
SAR VH	[20m 10km]	100 m	200 m	300 m	Noise	~1%
Airplane C5	[5m 100m]	15 m	30 m	50 m	~6%	Undef

Figure 5. (a) Similar to Figure 4a (transects of the observed surface roughness across the front) but note that the three horizontal axes do not have the same scales. To help the interpretation, Gaussian fits (with standard deviations in meters) are added as thin black curves. (b) Table summarizing the horizontal extensions and amplitudes of the observed roughness contrasts at the front. The roughness frontal width at 80% (resp. 50% and 20%) is defined as the spatial extension over which the roughness contrast (in absolute value) reaches more than 80% (resp. 50% and 20%) of the maximum contrast at the front.

current variations are thus traced in both VV and VH images. And cross-polarized images are thus correlated with copolarized images but are expected to exhibit weaker signatures at the front.

- The airplane observations, which cover spatial scales in the range [5m, 100m], exhibit the sharpest roughness contrast, with frontal width about 15 to 50m. The contrast also changes sign depending on the viewing geometry (Figures 3h and 3i), similarly to the MISR contrast.

3. Current Gradient From In Situ Observations

Before analyzing further the information contained in the surface roughness observations, we need to understand the underlying current gradient at the front. For that purpose, we turn toward available in situ observations.

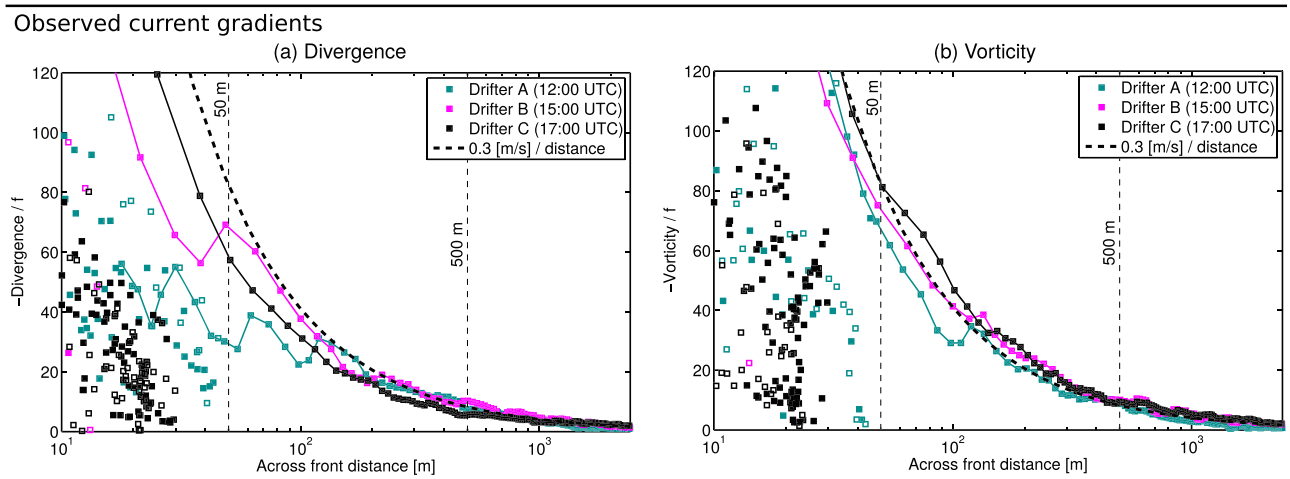

Figure 6. (a) Observed divergence and (b) vorticity between the front surface convergence zone and the three approaching Drifters A, B, and C, as function of their distance to the front. A simple velocity jump of $\Delta u = 0.3$ m s^{-1} is shown with the dashed black curve. Once caught within the front, the drifters experience random displacements around the front line, as shown by the clouds of points. Those displacements correspond to random positive (filled squares) and negative (open squares) current gradients. The vertical black dashed line at 50m shows a conservative maximum of those random excursions.

3.1. Front-Following Frame of Reference

The large number of surface drifters aligned within the front allows us to define a local frame of reference which follows the frontal convergence line. Nearby drifters (of the order of 5 to 10 drifters less than 2km away from the considered point) are used to define the front-following reference frame, with its origin taken as the center of mass of the drifters and the x axis (y axis) chosen across front (along front, respectively). Each velocity observation around the front is subsequently transformed into this local frame of reference. The resulting trajectories are shown in Figures 3a and 3d and in Movies S2 and S3. Note that no other treatment is done to the drifters trajectories, which therefore include all possible geophysical contributions (Stokes drift, windage, tides, etc.). In particular, the windage was quantified by Novelli et al. (2017) to less than 0.5% of the wind speed, which corresponds to 0.05 m s^{-1} during our experiment.

3.2. Surface Drifters

Most of the drifters (about 200) ended up aligned along the front direction and thus contain no information on the across-front structure of the current. This fast alignment due to current convergence or strain is a common sampling problem in the study of ocean fronts (Ohlmann et al., 2017). Fortunately, three Lone Drifters A, B, and C (Reference Numbers 2546407, 2545772, and 2545235) were redeployed outside of the front to sample the east side of the front at approximately 12:00, 14:00, and 17:00UTC, respectively (see red squares A, B, and C in Figure 2). The trajectories of Drifters A and C, within the local front-following reference frame, are shown in Figures 3a and 3d and in Movies S2 and S3.

The along-front and across-front velocities of the three lone drifters are shown in Figure 4b. The drifters are attracted toward the front at almost constant along-front and across-front velocities, about 0.3ms^{-1}. Once caught inside the convergence zone, surface drifters experience horizontal random displacements with a maximum extension of about 50m, which is shown as vertical black dash lines in Figures 3a, 3d, 3g, and 4b.

From the trajectories of those lone drifters, the current gradient can be calculated, as function of the distance to the front (Figure 6). The across-front velocity gradient corresponds to convergence, while the along-front velocity gradient corresponds to cyclonic vorticity (see Appendix A for details on the gradient calculations). The extreme sharpness of the front translates into extreme current gradients of about 50 to 100f, both for the convergence and for the cyclonic vorticity. This present result is fairly robust, as the three drifters (A, B, and C), reaching the front almost 5hr apart, exhibit very similar current gradients. Also, two different methods used to calculate the current divergence lead to similar orders of magnitudes (see Appendix A). Finally, a fourth Drifter D (Reference Number 2545209) reached the front minutes after Drifter A, at 12:30UTC, further south along the front (see red square D in Figure 2a). This Drifter D is not a lone drifter but is part

of secondary front being aggregated to the main front in a "zipper-like" convergent structure (see also D'Asaro et al., 2018). Despite the presence of this secondary front, current velocity jumps and current gradients calculated from Drifter D trajectory are similar to those of Drifters A, B, and C (and thus not shown in Figures 4b and 6).

Note that no drifters were redeployed on the west side of the front, which remains unsampled (Figures 3a and 3b). A weak converging current or an antisymmetrical current of equal magnitude as that of the east side are possible on the west side (Figure 4b) and would both be consistent with the drifter data. Possible differences between the current gradient on the east side compared to the west side of the front are illustrated in Appendix B (Figure B1), where the across-front current vertical circulation is based on the shallow tidal front observed by Lyzenga (1998).

3.3. Ship ADCP

The R/V Walton Smith was equipped with a 600 kHz hull acoustic Doppler current profiler (ADCP) and the data processed with an along-track resolution about 1 km (Shcherbina et al., 2013). The vessel crossed the northern part of the front at 08:05 and 08:43 UTC (Movie S1). Velocities (in the local frontal frame of reference) of the uppermost beams (at depths of 7 and 9 m) are shown in Figure 4c. Both across-front and along-front components of the velocities exhibit changes at the front, which are consistent with both cyclonic vorticity and convergence at the front. The magnitudes of the current jumps are about $0.2\,\mathrm{m\,s^{-1}}$ over 1 km, which corresponds to current gradients about $3f$, with f the local Coriolis frequency.

The vessel crossed again the frontal line further North at 09:20 and 10:15 UTC, where the ADCP exhibited less defined current gradients (not shown). The reason for such weak current gradients may be that the front was yet to strengthen in what appears to be its northern boundary at that time. This interpretation is supported by the weak SAR surface roughness contrast and by the inconsistent drifter trajectories in that region (Movie S1).

The vessel crossed the front for a fifth time at 12:25 UTC further south along the front, close to the "zipper-like" structure. This ship transect of the front occurred less than 5 min before and less than 500 m away from where Drifter D reached the front (red square D in Figure 2a). The ADCP shows velocity jumps about $0.5\,\mathrm{m\,s^{-1}}$ over 750 m (Figure 4c), which correspond to current gradients about $10f$ (see also D'Asaro et al., 2018, their Figure S9).

Whereas the current gradients are generally consistent between the drifters and the ADCP, the absolute values of current significantly differ. This cannot be attributed to time and space difference between the measurements, as the 12:25 UTC ship transect and the Drifter D trajectory are almost perfectly collocated in space and time. One notable difference is that the across-front component of the current does not change sign in the 08:05 and 12:25 UTC transects, in apparent contradiction with the surface drifter convergence and the definition of the front-following reference frame. This probably happens because the center of the vertical rotor (as, e.g., observed by Lyzenga, 1998, see next subsections and Figure B1) was at those times as shallow as 7 m and thus that the ADCP could not resolve the surface convergence. The vertical profiles measured by the ADCP seem to support this hypothesis (see Figures C1a and C1c). The along-front components measured by ADCP exhibit a large scatter between the different transects but remain roughly consistent with a cyclonic vorticity with a sign change of the current at the front. Differences between the drifters and the ADCP—in particular for the 08:05 and 08:43 transects having weak ADCP along-front currents on the positive side—might again indicate current vertical shear in the upper 7 m.

3.4. Ship X-Band Radar

The R/V Walton Smith was equipped with an X-band radar (Lund et al., 2018), which unfortunately did not start acquisitions until the next day at 01:48 UTC. The surface current was processed at a resolution of 500 m and exhibits current gradients consistent with convergence and cyclonic vorticity, with velocity jumps of the order of $0.2\,\mathrm{m\,s^{-1}}$ over 500 m, which corresponds to gradients about $3f$ (see Rascle et al., 2017, their Figure 5b).

3.5. Synthesis of the Observed Current Front

In the present case study, data from ADCP, X-band radar, and drifters at 500 m resolution show current gradients about 1 to $10f$ over 500 m (Figure 6). The available drifter data at higher resolution further show that

the current jump occurs over only 50 m, an order of magnitude less. This leads to current gradient 1 order of magnitude larger, about 10 to 100*f*.

Garvine (1979a, 1979b) proposed to distinguish between dissipative and rotating fronts, based on the ratio of a frictional length scale R_f to the baroclinic Rossby radius R_1. Submesoscale fronts are generally rotating fronts (see, e.g., McWilliams, 2016), as opposed to gravity fronts common around river plumes. The present front involves a density difference $\Delta\rho \simeq 1\,\mathrm{kg\,m^{-1}}$, with a vertical thickness $D \simeq 30$ m of the light layer. The baroclinic Rossby radius is thus $R_1 = \sqrt{g' D}/f \simeq 7$ km, where g' is the reduced gravity. The frictional length scales as $R_f = D/a$ but is subject to uncertainty about the rate of entrainment, parameterized with the coefficient a, with suggested values varying from 1.7×10^{-2} to 3×10^{-3} (Garvine, 1979b). The frictional length scale R_f would thus range between 2 and 10 km. The present front thus exhibits a ratio $R_f/R_1 \simeq 1$, indicating that both friction and rotation are important.

3.6. Previously Documented Submesoscale Fronts

Many measurements around submesoscale fronts have already been reported in the literature. Most estimates report current gradients about 1 to 10*f* over 500 m. For instance, Flament and Armi (2000) documented a filament with cyclonic vorticity of 3*f* and convergence of 0.5*f* at 2 km resolution. They also suggested that gradients greater than 7.5*f* would be obtained at higher (80 m) resolution. More recently, Ohlmann et al. (2017) documented fronts and eddies with convergence/divergence and cyclonic vorticity about 5 to 10*f* over 300 m. Matthews and Yoshikawa (2012) used satellite along-track stereo imagery to calculate surface displacements of slicks between two consecutive images. Their results indicated current fronts less than 100 m wide, but no in situ measurements could confirm those values. Our present observations suggest current gradient values much larger than previously documented ones, for submesoscale fronts of this length (more than 10 km) and depth ($D \simeq 30$ m, D'Asaro et al., 2018).

3.7. Previously Documented Nonrotating Shallow Fronts

Large observed values of current gradients are more typical of gravity current fronts at river plumes, which are much shallower, of smaller horizontal scale and less influenced by the Earth rotation than dissipation (i.e., $R_f \ll R_o$; see, e.g., Garvine, 1974). For instance, Garvine and Monk (1974) reported measurements of a plume about 2 m deep, exhibiting 20 m wide front with current jump $\Delta u \simeq 0.5\,\mathrm{m\,s^{-1}}$. Although rotation is not important for that front, for comparison purpose we note that this corresponds to a current gradient about 300*f*. Marmorino and Trump (1996) measured another shallow tidal front, with $D \simeq 5$ to 10 m, front width about 6 m, and current gradient about 400*f*. O'Donnell et al. (2002) reported measurements of a plume about 5 m deep, front width about 5 m wide and current gradients about 1,000*f*.

Simpson and Britter (1979) proposed in the case of gravity currents that the frontal width is of the order of a few times the thickness of the dense layer D. The aforementioned river plume fronts are much shallower than the front described here ($D \simeq 5$ to 10 m instead of 30 to 40 m).

3.8. Previously Documented Fronts of Similar Scales

Marmorino and Trump (1994) reported observations of slightly deeper gravity current fronts ("bore-like") at the Gulf Stream boundary, with a layer $D \simeq 10$ m of light shelf water propagating over the Gulf Stream water in relatively shallow parts of the shelf (bottom depth about 30 m). Rotor like circulation, with frontal width about 50 m and current gradients up to 200*f*, was suggested by Lyzenga (1998) by analogy with the frontal rotor observed by Luketina and Imberger (1987) at a shallower (5 m) river plume. This rotor circulation proposed by Lyzenga (1998) is presented in Appendix B (Figure B1). Although direct in situ measurements of currents were lacking, lower-resolution ADCP currents and ship GPS tracks indeed suggested velocity jumps at the front $\Delta u \simeq 0.5\,\mathrm{m\,s^{-1}}$. Hydrographic sections suggested frontal width about 20 m and ADCP backscatter depth supported this vertical interpretation in terms of rotor (Marmorino et al., 1999). The correspondingly large current gradients about 200 to 300*f* helped Jansen et al. (1998), Lyzenga (1998), and Marmorino et al. (1999) to get agreement between observed and modeled NRCS anomalies of airborne radars at different wavelengths. The rotating nature of those bore-like fronts is uncertain, as Lyzenga (1998) neglects the along-front current in their modeling while Jansen et al. (1998) propose a cyclonic shear at the front.

The present observations support similar conclusions in terms of horizontal scale (50 m) and current gradient (100*f*), for a deeper front and with direct observation of current using the drifters. The along-front

component of the current, which shows cyclonic vorticity of similar amplitude as the convergence, is also better documented. The presence of a jet in the along-front component, which Garvine (1979b) suggests as a key difference between rotating and dissipative fronts, cannot be completely ruled out because drifter observations are only available on one side of the front (Figure 4b) but appear unlikely from the ADCP observations (Figure 4c), as was the case for the front observed by Marmorino et al. (1999).

4. Current Gradient From Surface Roughness Observations

Given the in situ evidence that the current gradient occurs over only 50 m, the question arises as to how such sharp current gradient can be traced and estimated by surface roughness observations.

4.1. Spatial Extension of the Roughness Anomaly

A localized surface current gradient generates a localized modulation of surface wave action, which translates into a local anomaly of surface wave mean square slope (mss). Image brightness intensity B (for sunglint images) or radar cross section σ (for SAR images) are quantities related to the mss (e.g., Kudryavtsev et al., 2012b).

Note that the typical surface wave scales affected by surface current variations can be evaluated. Following Equation 2 given in Kudryavtsev et al. (2012b), for a surface current width of 50 to 100 m, most impacted surface waves are short gravity waves with wavelengths in the range 10 to 15 m, for a wind speed of 9 m s^{-1}.

If the wave action N is split into a slowly varying background and a small local anomaly, $N(\vec{k}, \vec{x}) = N_0(\vec{k}) + N'(\vec{k}, \vec{x})$, the conservation of wave action for the anomaly gives (e.g., Phillips, 1984, their equation 3.1)

$$\left(c_{gi} + u_i\right)\frac{\partial N'}{\partial x_i} = k_j \frac{\partial u_j}{\partial x_i}\frac{\partial N_0}{\partial k_i} - \frac{N'}{\tau_c}, \tag{1}$$

where $\vec{x} = (x_1, x_2)$ is the position, $\vec{u}$ is the surface current, $\vec{k}$ the wavenumber, $\vec{c_g}$ the group velocity, and repeated indices indicate summation over the two horizontal components. $\tau_c(\vec{k})$ is the relaxation time scale, which is the e-folding time needed by waves to reach back their equilibrium with the local wind (e.g., Alpers & Hennings, 1984, their equation 8). The first term on the right-hand side (rhs) is the source of action due to local current gradient. The second term on the rhs is the restoring force toward the equilibrium with the local wind. The left-hand side (lhs) is the propagation/advection of wave energy. If the propagation/advection is negligible, the horizontal extension of the wave action anomaly (i.e., the roughness frontal width) exactly matches the current gradient frontal width.

On a surface roughness image, the roughness frontal width is thus expected to be larger than the current gradient frontal width because of two processes: (i) the propagation/advection of wave energy (lhs of Equation 1) and (ii) the instrument resolution, which acts as a spatial low-pass filter.

4.2. Numerical Simulation

Those two processes are quantified here using numerical simulations with the model of Kudryavtsev et al. (2005). The model simulates wind waves propagating over a current gradient by solving the linearization of the conservation of wave action 1. The horizontal spatial resolution is 1 m. Waves with wavelengths from 1 mm to 100 m are resolved, with a spectral grid of 100 logarithmically spaced wavenumbers and 80 directions. The background waves are supposed fully developed. The wave spectrum N_0 is set to the form given by Dulov and Kudryavtsev (1990) for the energy containing waves, while shorter waves in the equilibrium range are set by an energy balance equation (see Kudryavtsev et al., 2005, for more details). The wind is set to 9 m s^{-1} at an angle of 45° with the front, in agreement with observations from a nearby meteorological buoy (National Data Buoy Center Station 42040), which reported a wind about 9 m s^{-1} from WSW (255°).

The model is run with a current mimicking the observations (Figure 4b), namely,

$$u(x) = -\frac{\Delta u}{2}\left(1 + \tanh\frac{3x}{L_u}\right), \quad v(x) = -u(x), \tag{2}$$

where the velocity jump Δu takes values between 0.1 and 0.6 $\mathrm{m\,s^{-1}}$ and the current length scale L_u values between 30 and 3,000 m. The resulting amplitudes of the mss contrast at the front are shown in Figures 7a and 7b as function of L_u and Δu.

4.3. Range of Roughness Horizontal Scales

Each instrument is sensitive to a limited range of roughness horizontal scales. The lower bound is set by the instrument resolution. The upper bound is set by the restriction on varying view geometry (see section 2.3). The mss anomaly calculated by the model is thus spatially band-pass filtered in the range of wavelengths detected by the airplane (Figure 7a) and by MISR (Figure 7b) before calculating the mss contrasts.

Three specific runs are highlighted to discuss the model results (Figure 7d), with Run #1 a low-resolution current (L_u=500 m) and Runs #2 and #3 realistic high-resolution currents (L_u=50 m). The spatial power spectra of the imposed current gradients (Equation 2) are shown in black in Figure 7c for the Runs #1 and #2, while the spectra of the corresponding mss contrasts calculated by the model are shown in cyan. As expected, by considering wave propagation/advection in Equation 1, the mss response involves longer horizontal wavelengths than those of the imposed current gradient (Figure 7c, see shift between corresponding black and cyan curves).

To note, without considering the propagation/advection and the limited range of scales resolved by the instrument, the amplitude of surface roughness contrast can be simply evaluated with the rhs of Equation 1. In this approximation, Kudryavtsev et al. (2012b) showed the mss contrast to be a function of wind speed U_{10}, current velocity jump Δu, and spatial extent of current gradient L_u, as

$$\frac{mss'}{mss} \sim \frac{\Delta u}{U_{10}}\frac{l_c^{1/2}}{L_u^{1/2}}, \tag{3}$$

where l_c a fixed length scale. Accordingly, a decrease of L_u by a factor 10, from Run #1 to Run #2, for instance, would give an increase of the surface roughness contrast by a factor $\sqrt{10}\simeq 3.16$. This approximation barely holds for the mss contrast at scales in the range [275 m, 10 km] (see horizontal dashed red line in Figure 7b, the contrast increase between Run #1 and Run #2 is 150%, instead of the 316% predicted by 3). And the approximation completely fails for mss contrast in the range [5 m, 100 m] (see Figure 7a, the contrast increase between Run #1 and Run #2 is more than 1,000%, instead of the 316% predicted). The impact of the band-pass filtering completely invalidates the approximation 3 in that range of scales. In other words, due to the band-pass filtering, Run #1 should produce very small mss contrasts in the range [5 m, 100 m], much less than the 5% expected using 3.

This is a first important result: The range of spatial scales resolved by the roughness instrument plays a crucial role for the interpretation surface roughness observations and is not present in simplified models like 3.

4.4. Current Gradient Estimation From Airplane Observations

Surface roughness measured from our airplane is restricted to horizontal scales in the range [5 m, 100 m]. The model predicts that fronts with L_u>200 m could not be detected by the instrument, as they would produce weak mss contrasts (<1%, see, e.g., Run #1 in Figures 7a and 7c). On the contrary, fronts with $L_u\simeq$50 m should be well estimated by the airplane observations (see Run #2 in Figures 7a and 7c).

Inversion of model runs to match observed values of roughness frontal width (Figure 5b) leads to values of L_u about 30 to 50 m (see model frontal widths in Figure 7d), in good agreement with the drifter observations. Subsequent inversion of model runs to match observed values of the amplitude of the roughness contrast leads to values of Δu about 0.2 to 0.3 $\mathrm{m\,s^{-1}}$ (Figure 7a), again in good agreement with drifter observations. This estimation gives current gradients $\Delta u/L_u$ in the range 70 to 110*f*. Note that the estimation of the current jump Δu is fairly sensitive the estimation of L_u (the roughness contrast predicted by the model presents a steep slope for $L_u\sim$50 m, Figure 7a) and thus subject to large errors. On the contrary, the current gradient $\Delta u/L_u$ is less sensitive to L_u and rather sensitive to the value of the roughness contrast at the front.

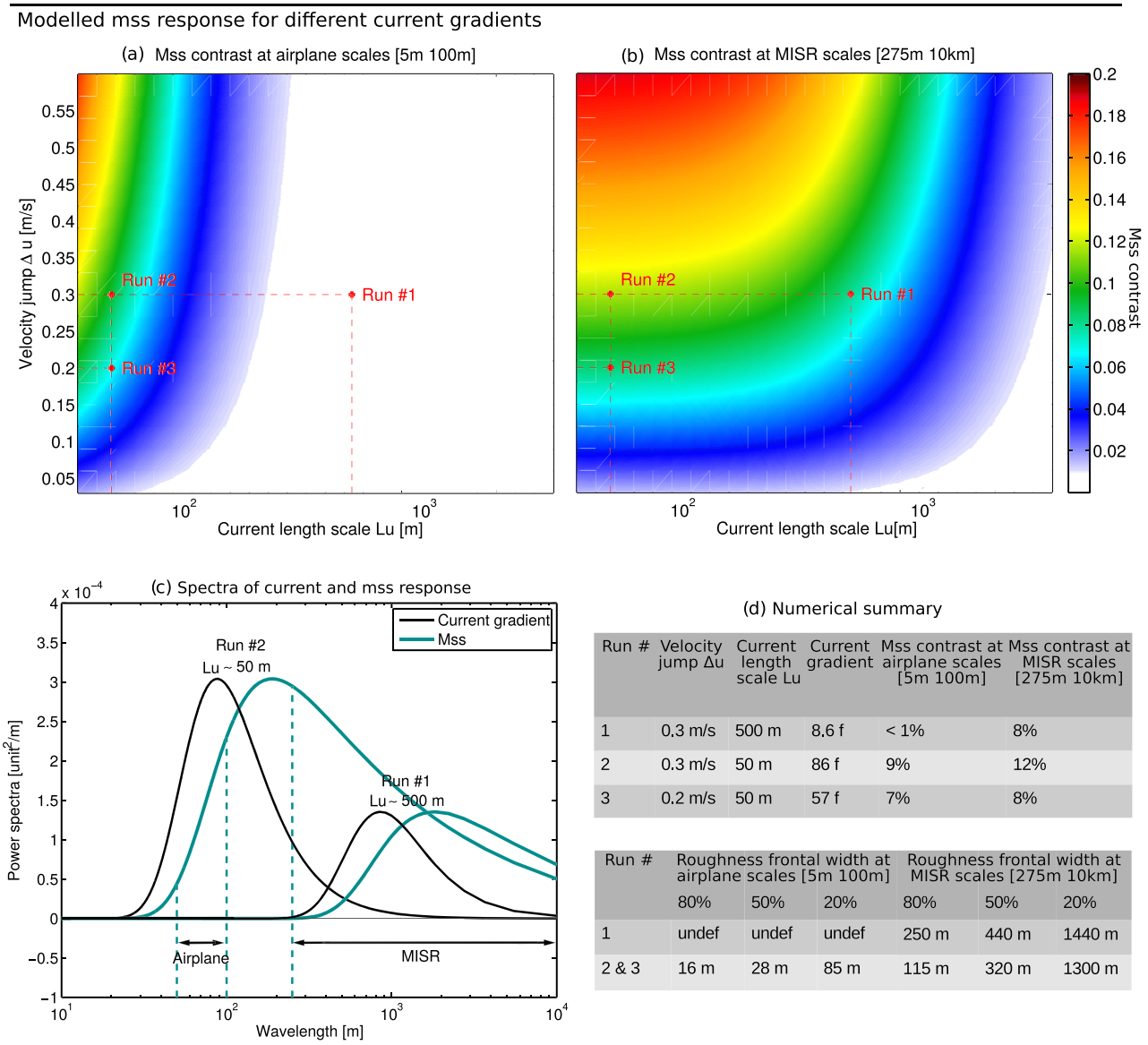

(d) Numerical summary

Run #	Velocity jump Δu	Current length scale Lu	Current gradient	Mss contrast at airplane scales [5m 100m]	Mss contrast at MISR scales [275m 10km]
1	0.3 m/s	500 m	8.6 f	< 1%	8%
2	0.3 m/s	50 m	86 f	9%	12%
3	0.2 m/s	50 m	57 f	7%	8%

Run #	Roughness frontal width at airplane scales [5m 100m]			Roughness frontal width at MISR scales [275m 10km]		
	80%	50%	20%	80%	50%	20%
1	undef	undef	undef	250 m	440 m	1440 m
2 & 3	16 m	28 m	85 m	115 m	320 m	1300 m

Figure 7. (a) Amplitude of the modeled mss response at scales in the range [5m, 100m], as function of the imposed current length scale L_u and velocity jump Δu. Location of the Runs 1, 2, and 3 are highlighted with the red dashed lines. (b) Same as (a) but for scales in the range [275m, 10km]. (c) Spatial power spectra of the current gradient $\partial u/\partial x$ (black curves) and of the corresponding mss contrast (cyan curves), for the numerical model Runs #1 and #2. The ranges of scales observed by airplane and by MISR are also shown with double head arrows. Note that for display purposes, each spectrum of mss response has been normalized to match the maximum value of the corresponding imposed current spectra. (d) Summary of the numerical results for the three specific model Runs #1, #2, and #3.

4.5. Current Gradient Estimation From MISR Observations

Surface roughness measured from MISR is restricted to horizontal scales in the range [275m, 10km]. The unexpected result is that the actual front, although much sharper than 275m, is detected by the instrument. This is consistent with the model prediction of nonnegligible mss contrast (see, e.g., Run #2 in Figures 7b and 7c). The wave propagation/advection is likely contributing to widen the mss contrasts over an area larger than the intense current gradient region. Nonetheless, though the front is detected by the instrument, it is very difficult to correctly assess its length scale L_u, given the large mismatch between the actual current scale ($L_u \simeq 50$m) and the instrument resolution (275m). As a numerical illustration, model estimations of L_u are above 500m, probably up to 1,500m, to match the observed roughness frontal widths (Figure 5b).

This is much larger than the drifters observations of $L_u \simeq 50$m. This indicates either insufficient wave propagation/relaxation in the model or that the MISR effective resolution is not properly modeled by a low-pass cutoff at 275m.

As MISR cannot correctly estimate the current length scale L_u, estimations of current jump Δu are also incorrect, with corresponding values from 0.3 to more than $1.5\,\mathrm{m\,s^{-1}}$. This would lead to current gradient in the range 7 to 15f, much below the observations. Therefore, due to the large mismatch between the actual current scale L_u and the instrument resolution, MISR cannot correctly estimate the current gradient. This is illustrated differently with Runs #1 and #3: Both produce similar mss contrasts about 8% (Figures 7b and 7d) despite having an order of magnitude between their length scales L_u. The only way to distinguish them would be through their roughness frontal widths, which unfortunately is very difficult to estimate (it appears in both cases greatly underestimated; cf. modeled frontal width of Figure 7d to observed frontal width of Figure 5).

The general conclusion of that numerical study is that both (i) the wave propagation/advection and (ii) the band of spatial wavelengths resolved by the roughness instrument are critical to retrieve the current gradient from surface roughness observations. This is further illustrated in Figure 5. Assuming that the MISR observation would simply be a 275m low-pass filter of the airplane observation would lead to a roughness contrast reduction from 8% (airplane) to 0.8% (MISR), as given by the convolutions of two Gaussians with standard deviations of 30 and 275m. This is clearly below the observed 5% (MISR), most likely because roughness variations in the scale range [100m, 275m] (created by the wave propagation/advection) are missed by both instruments.

4.6. Current Gradient Estimation From SAR Observations

Surface roughness measured by Sentinel-1 in theory covers horizontal scales in the range [20m, 10km]. However, as mentioned above, the inherent speckle noise limits the effective resolution of the SAR instrument to probably 100 or 200m (Figure 2b). The NRCS contrast σ'/σ in the range [20m, 100m] is thus mostly noise, the contrast in the range [275m, 10km] is about 5% and most of the observed contrast (up to 40%, Figure 5a) clearly occurs in the range [100m, 275m], which are the shortest identifiable spatial scales. The large contrast observed at scales smaller than 275m should be an indication that the current length scale L_u is also smaller than 275m, in agreement with the drifter observations. We note, however, that inversion of the NRCS (detected by a microwave SAR) into a current gradient is not as straightforward as the inversion of the mss (detected by optical radiometers). The NRCS contrast follows a more complex dynamics than the mss, because it involves the sum of a polarized Bragg-scattering term plus a scalar contribution associated with wave breaking, both of which having potentially different relaxation scales. Our observations took place with the SAR azimuth look direction at about 45° of the wind direction, a slanting angle at which wave breaking is believed to generate a nonnegligible fraction of the Bragg scatterers (see Kudryavtsev et al., 2012b, their Equation 6), which brings in additional uncertainty to interpret the NRCS contrast. Those uncertainties can be reduced if quad polarization (VV, VH, HV, and HH) is available (Kudryavtsev et al., 2014), which is unfortunately not the case in our observations, where only the VV polarization has a significant signal to noise ratio.

5. Discussion and Applications

5.1. Frontal Currents

The combination of in situ and remotely sensed observation helps building a quasi-complete picture of surface currents in the vicinity of the present front. Drifter trajectories reveal almost step-like current variations on the dense side the front, both for the convergent across-front component and for the cyclonic along-front component. Those current jumps occur within less than 50m, which is also the maximum size of horizontal excursions of drifters once caught within the convergent line. It suggests that this could be the relevant length scale of instabilities responsible for frontal arrest. The light side of the front was not sampled by drifters, leaving open the possibilities for gradients on that side that could be weaker, stronger, or even of opposite signs, with divergence or anticyclonic vorticity with an horizontal jet at the front. Ship ADCP transects across the front at different times and locations provide information on both sides of the front but at lower spatial resolution. They seem to confirm the convergent and cyclonic current jumps and show no evidence of

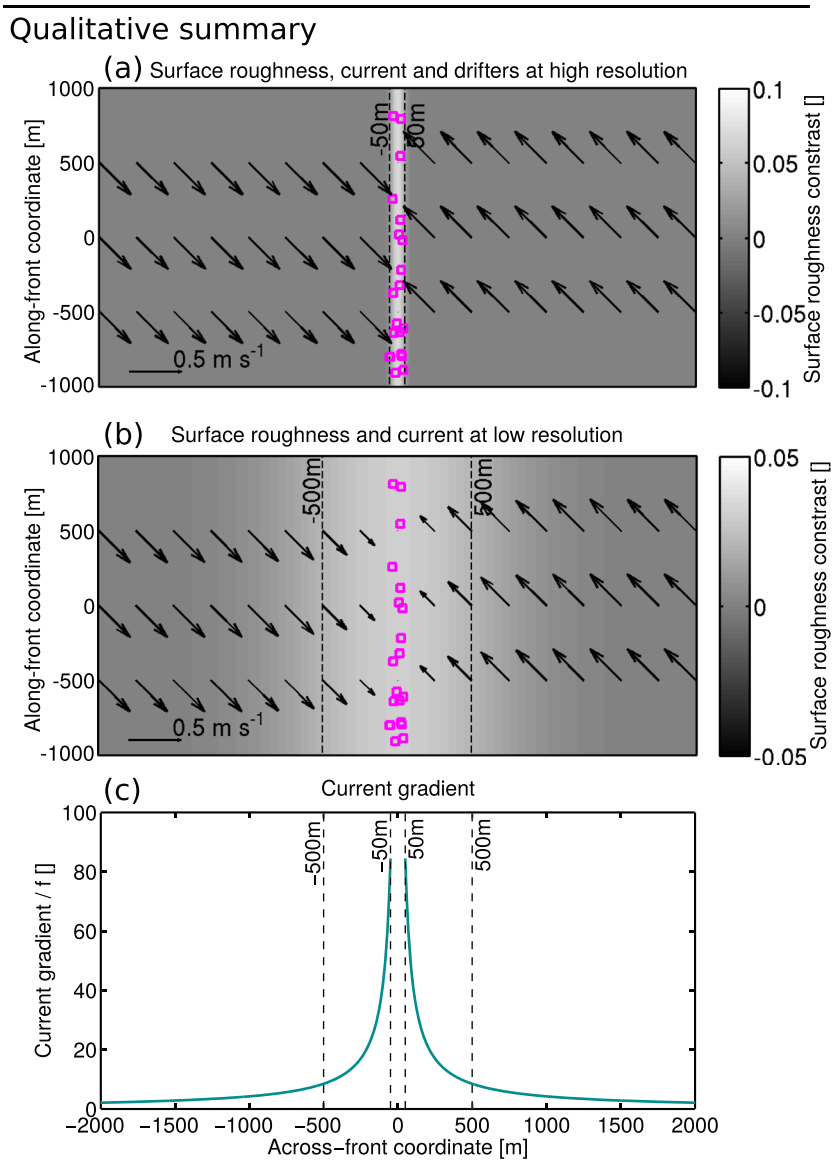

Figure 8. Qualitative illustration to summarize the results. (a) A very sharp front was consistently detected by high-resolution surface roughness (from airplane sunglint and SAR) and drifters. (b) Lower-resolution surface roughness (MISR) can also detect the front and can provide the drifter locations at reduced accuracy and precision. (c) Frontal currents as inferred from 500 m resolution sensors (e.g., MISR sunglint, ship ADCPs, and shipborn X-band) would have gradients of the order of 10*f*, an order of magnitude below the observations at high resolution (e.g., by airplane sunglint and surface drifters). Note that gradients are defined here as averaged gradients between point considered and the front.

a change of sign of the gradients at that resolution. In turn, surface roughness images at the highest resolution (from the airplane and from the SAR) confirm the location of the strongest current gradient within less than 50 m of the convergence line. If divergence exist on the front side unsampled by the drifters, it is sufficiently weak not to appear on roughness images and occurs at scales sufficiently short not to appear on ADCP data. The same conclusion goes for the eventual presence of a jet with anticyclonic vorticity on the unsampled side.

5.2. Ideal Instrument

A sensor at high resolution is needed to successfully estimate sharp current gradients at such fronts. As discussed, a sensor at low resolution (like MISR) can detect both smooth current gradients (e.g., Run #1) and—

thanks to wave propagation/advection and to the instrument spatial filtering—sharp current gradients (e.g., Run #3), but it can hardly discriminate between them, contrary to a sensor at high resolution (like our airplane radiometer). This demonstrates that, in addition to locate the front precisely (section 2.4), a high-resolution sensor is necessary to accurately estimate the current gradient at the front.

Due to their high altitude, satellite sensors have the advantage of covering large scales without too much change in the viewing geometry (we limited MISR and Sentinel-1 to 10 km scales, as discussed in section 2.3). Under clear-sky conditions, multiangular optical instruments with 10 m pixel resolution would be ideal (e.g., Kudryavtsev et al., 2017). Using all-weather high-resolution radar observations, polarization sensitivity is necessary to quantitatively separate the measured roughness variations between changes associated with denser breaking patches and purely resonant short-scale scatter modulations, that is, to separate effects associated with surface currents and wind variability (Kudryavtsev et al., 2014). In particular at moderate wind speed, breaking waves have relatively small relaxation scale (about 5 to 100 m) and can thus precisely locate the intense surface current variations.

5.3. Geophysical Applications

This paper demonstrates the possibility of detecting and quantifying strong current gradients from surface roughness observations. This opens new possibilities to study the dynamical mechanisms at play around submesoscale fronts, including oceanic, atmospheric, or wave-related mechanisms. Future applications could include the following:

- *Identification of the precise location of accumulated drifting material*. The near-real-time availability of surface roughness images could be useful for operational purposes related to pollution or search and rescue.
- *Discrimination between "active" and "fossil" submesoscale fronts*. Numerous SST fronts are found within the northern Gulf of Mexico. Some are compensated by salinity, leading to weak density front and weak current gradient at the front. The absence of surface roughness anomaly is an indication that the front has a low dynamical activity and could be coined as inactive or "remnant" or "fossil."
- *Identification of the areas of current gradient intensification within submesoscale features*. For instance, in the case of the studied spiraling eddy, the satellite image of Figure 1b suggests that the spiral is composed of two main arms, one in the northwest of the eddy and one in the southeast. Furthermore, the image of Figure 2b suggests that the northwest arm presents intensified current gradient in its westernmost section and that the gradients are weaker closer to the core of the eddy and further away from it.
- *Improvement of the resolution of current remote sensing*. Surface roughness provides information on current gradients at very high resolution. This information should be viewed as a complement to absolute currents obtained at lower resolution with other techniques. For instance, the future Surface Water and Ocean Topography (SWOT) mission (Fu et al., 2012) will provide currents at about 20 km resolution using sea surface height observations (as in conventional altimetry). The complementary use of the NRCS (σ in our notations) of the instrument at 250 m resolution should help reconstructing currents at a resolution higher than 20 km (see Morrow et al., 2019, their Figure 7). Similar reconstruction could be performed as well on the absolute currents provided by the future Wind and Current Mission (WaCM) based on the Doppler scatterometer concept (Rodríguez et al., 2018) or on the absolute currents provided by any other technique (e.g., along track stereo imagery, Matthews & Yoshikawa, 2012).

6. Summary

This paper presents combined observations of an intense submesoscale front, including in situ current measurements and remotely sensed surface roughness. This set of observations is quite exceptional, combining numerous drifters and numerous instruments detecting surface roughness at different scales. A graphical summary is proposed in Figure 8.

A first surprise is the sharpness of the front. Submesoscale frontal currents are usually depicted as occurring over scales about 100 m to 1 km, with current gradients documented up to 10*f*. The front described here, despite being elongated over more than 10 km, is only about 50 m wide, as demonstrated from drifters trajectories. This leads to current gradients up to 100*f*, an order of magnitude larger than previously documented ones.

Fronts with such intense current gradients produce intense surface roughness anomalies, which can be used to monitor them. Because of the wave relaxation, surface roughness anomaly may occur over larger spatial scales than the current gradient. The front can thus be detected by instruments with spatial resolution much larger than the front width, as demonstrated here with the MISR sensor and numerical modeling. However, those instruments can hardly discriminate between sharp fronts (with strong current gradients) and wide fronts (with weak current gradients). On the contrary, airplane observations demonstrate that a high-resolution sensor can more correctly estimate the width and strength of the current gradient, while indeed being also able to detect the location of accumulated drifting material with a high spatial accuracy.

This demonstrates the possibility to accurately monitor intense frontal current gradients from surface roughness observations and imposes a strong constraint on sensors to detect and quantitatively interpret those "storms below the ocean surface."

Appendix A: Current Gradient Calculations From the Drifters

Current gradient from the drifter trajectories are calculated using two independent methods, with very similar results.

The first method uses the relative trajectory of one approaching drifter (Drifter A, B, or C) compared to the average position of the front defined by other nearby drifters already trapped in the convergence zone. We assume a nearly infinite rectilinear front with no variation in the y direction. The current gradient thus has two components, across-front $\partial u/\partial x$ and along-front $\partial v/\partial x$, which identify with divergence and vorticity. Those components can be simply calculated as $\partial u/\partial x \simeq u(x)/x$ because the frame of reference is located on the front. This is the method applied in Figure 6.

The second method uses triplets of drifters, including one approaching drifter (A, B, or C) plus two nearby drifters already trapped in the front. We then average over the possible triplets (10 to 55 triplets if 5 to 10 nearby drifters are chosen). This second method is much noisier but does not make the assumption of a rectilinear front. The results are shown in Figure A1for the divergence, obtained as the normalized rate of change of the drifter triplet area $\mathscr{A}$ (Molinari & Kirwan, 1975; Okubo et al., 1976),

$$\frac{\partial u}{\partial x}+\frac{\partial v}{\partial y}=\frac{1}{\mathscr{A}}\frac{d\mathscr{A}}{dt}. \tag{A1}$$

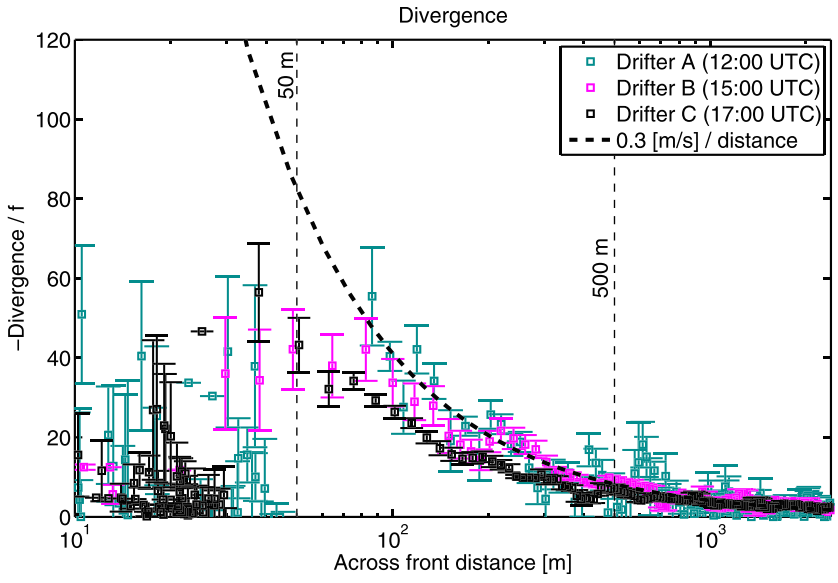

Figure A1. Similar to Figure 6a but the divergence is calculated using triplets of drifters and their area rate of change. The mean and its standard error over the possible triplets are shown.

To discard nearly aligned drifters, triplets with an aspect ratio (defined as the ratio of the circumradius to twice the inradius) superior to 50 are omitted, a criterion similar to that used by Ohlmann et al. (2017). The mean and standard deviation over the remaining triplets are shown in Figure A1 and shows divergence reaching up 40*f* at 50 m from the front, before noise and triangle aspect ratios become too large. This divergence is of similar order than that obtained with the first method, which gives about 50*f* at 50 m from the front.

Appendix B: An Example of Vertical Circulation Observed at a Tidal Plume Front

Lyzenga (1998), Marmorino et al. (1999), and Jansen et al. (1998) discussed observations of a nonrotating front along a tidal plume by Marmorino and Trump (1994). The observed vertical stream function, surface across-front current, and the resulting divergence are shown in Figure B1. Here all currents are translated to the frame of reference of the surface convergence zone, the "front" where hypothetical surface drifters would gather. In their case, the current gradient is not symmetrical about the front, with the trailing edge (left side) experiencing larger gradients.

Appendix C: Vertical Circulation at the Front Observed by ADCP

In support of Figure 4c which shows the uppermost two beams of the ship ADCP at 7 and 9 m, the full vertical profiles of the current along the transects across the front at 08:05, 08:43, and 12:25 UTC are shown in Figure C1. For comparison purposes, a velocity jump of 0.3 m s^{-1} at 50 m of the front is shown on the front positive side, which corresponds to the side sampled by Drifters A, B, C, and D. By definition of the front-following reference frame, both components (across and along front) of the velocity should become 0 at the front. An across-front vertical rotor like that of Figure B1 most likely explains why the ADCP across-front current is nonzero at the front.

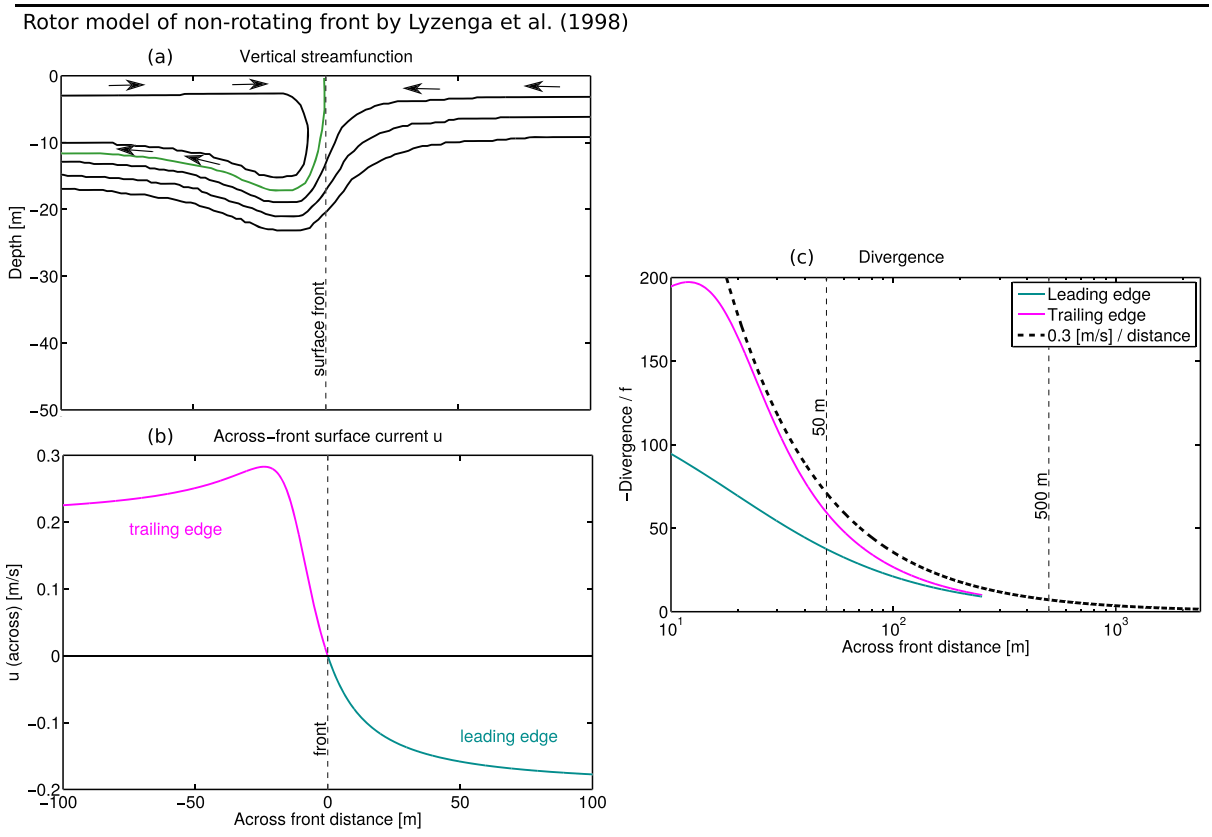

Figure B1. Analytical fit by Lyzenga (1998) to the tidal plume front observed by Marmorino et al. (1999). (a) Vertical stream function. (b) Across-front surface current. (c) Divergence between the frontal surface convergence zone and a distance from the front.

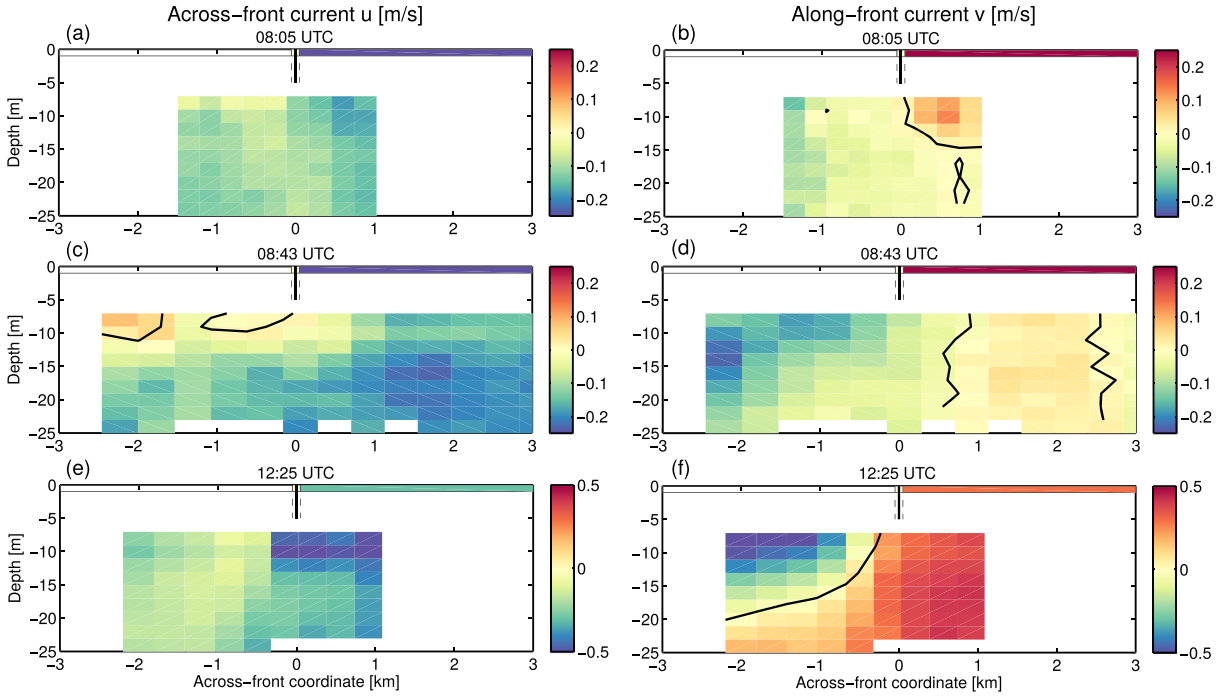

Figure C1. Vertical transects of currents measured by ship ADCP during front crosses at 08:05, 08:43, and 12:25UTC. Velocities are defined in local front-following frame of reference, defined by nearby (less than 2km away) drifters caught within the front. Thick vertical black line in the depth range [0, 5 m] shows the surface position of the front, as defined in that frame. Thin dashed vertical black lines indicate ±50m from the front. The ADCP measures current at depth greater than 7m. Thick black contour indicate the zero measured by the ADCP. For comparison purposes, velocity jumps of $0.3\,\mathrm{m\,s^{-1}}$ at +50m of the front are also shown in the depth range [0, 1m], as approximately observed from the trajectories of Drifters A, B, C, and D.

Data Availability Statement

All data are publicly available through the Gulf of Mexico Research Initiative Information and Data Cooperative (GRIIDC) at https://data.gulfresearchinitiative.org at DOI: 10.7266/N7CR5RT5 (airborne roughness data), DOI: 10.7266/N7N01550 (X-band radar data), DOI: 10.7266/N7MS3R6V (surface drifters data), and DOI: 10.7266/N7S75DRP (shipborne ADCP data).

Acknowledgments

N. R. and J. M. were supported by LabexMER via Grant ANR-10-LABX-19-01. We also acknowledge the financial support from CNES (Centre National d'Etudes Spatiales) of the ANR (French Agence Nationale pour la Recherche) through the REDHOTS project and of the ESA (European Space Agency) through the STSE MESO3D project, the GlobCurrent-WOC project, and the SARONG project. This research was made possible in part by a grant from The Gulf of Mexico Research Initiative. We thank Olivier Ménage for his help to set-up the cameras. We used the website http://lance-modis.eosdis.nasa.gov to download the Level-1 MODIS data. We thank Emmanuelle Autret for computing the brightness temperature data. We thank Tamay M. Özgökmen, Andrey Shcherbina and Eric D'Asaro for their help with the CARTHE-LASER data. We thank John P. Matthews and 4 anonymous reviewers for their useful comments during the GRL / JGR review process.

References

Alpers, W. (1985). Theory of radar imaging of internal waves. *Nature*, *314*(6008), 245–247.

Alpers, W., & Hennings, I. (1984). A theory of the imaging mechanism of underwater bottom topography by real and synthetic aperture radar. *Journal of Geophysical Research (1978–2012)*, *89*(C6), 10,529–10,546.

Apel, J. R., Byrne, H. M., Proni, J. R., & Charnell, R. L. (1975). Observations of oceanic internal and surface waves from the Earth Resources Technology Satellite. *Journal of Geophysical Research*, *80*(6), 865–881.

Chust, G., & Sagarminaga, Y. (2007). The multi-angle view of MISR detects oil slicks under Sun glitter conditions. *Remote sensing of Environment*, *107*(1), 232–239.

Cooper, A. L., Shen, C. Y., Marmorino, G. O., & Evans, T. (2005). Simulated radar imagery of an ocean“ spiral eddy ”. *IEEE transactions on geoscience and remote sensing*, *43*(10), 2325–2331.

D'Asaro, E. A., Shcherbina, A. Y., Klymak, J. M., Molemaker, J., Novelli, G., Guigand, C. M., et al. (2018). Ocean convergence and the dispersion of flotsam. *Proceedings of the National Academy of Sciences*, *115*(6), 1162–1167.

Diner, D. J., Bruegge, C. J., Martonchik, J. V., Ackerman, T. P., Davies, R., Gerstl, S. A. W., et al. (1989). MISR: A multiangle imaging spectroradiometer for geophysical and climatological research from EOS. *IEEE Transactions on Geoscience and Remote Sensing*, *27*(2), 200–214.

Dulov, V., & Kudryavtsev, V. (1990). Imagery of the inhomogeneities of currents on the ocean surface state, Soviet. *Journal of Physical Oceanography*, *1*(5), 325–336. https://doi.org/10.1007/BF02196830

Eldevik, T., & Dysthe, K. B. (2002). Spiral eddies. *Journal of Physical Oceanography*, *32*(3), 851–869.

Fedorov, K. N. (1986). *The physical nature and structure of oceanic fronts*. New York Inc., New York, NY: Springer-Verlag.

Ferrari, R., & Rudnick, D. L. (2000). Thermohaline variability in the upper ocean. *Journal of Geophysical Research*, *105*(C7), 16,857–16,883.

Flament, P., & Armi, L. (2000). The shear, convergence, and thermohaline structure of a front*. *Journal of Physical Oceanography*, *30*(1), 51–66.

Fu, L. L., Alsdorf, D., Morrow, R., Rodriguez, E., & Mognard, N. (2012). SWOT: The Surface Water and Ocean Topography mission: Wide-swath Altimetric measurement of water elevation on Earth. *Jet Propulsion Laboratory JPL-Publ*, *12-05*, 1–228. available at http://hdl.handle.net/2014/41996

Garvine, R. W. (1974). Dynamics of small-scale oceanic fronts. *Journal of Physical Oceanography*, *4*(4), 557–569.
Garvine, R. W. (1979a). An integral hydrodynamic model of upper ocean frontal dynamics: Part I. Development and analysis. *Journal of Physical Oceanography*, *9*(1), 1–18.
Garvine, R. W. (1979b). An integral hydrodynamic model of upper ocean frontal dynamics: Part II. Physical characteristics and comparison with observations. *Journal of Physical Oceanography*, *9*(1), 19–36.
Garvine, R. W., & Monk, J. D. (1974). Frontal structure of a river plume. *Journal of Geophysical Research*, *79*(15), 2251–2259.
Grimes, C. B., & Finucane, J. H. (1991). Spatial distribution and abundance of larval and juvenile fish, chlorophyll and macrozooplankton around the Mississippi River discharge plume, and the role of the plume in fish recruitment. *Marine ecology progress series. Oldendorf*, *75*(2), 109–119.
Jackson, C., & Alpers, W. (2010). The role of the critical angle in brightness reversals on sunglint images of the sea surface. *Journal of Geophysical Research*, *115*, C09019. https://doi.org/10.1029/2009JC006037
Jackson, C. R., da Silva, J. C. B., Jeans, G., Alpers, W., & Caruso, M. J. (2013). Nonlinear internal waves in synthetic aperture radar imagery. *Oceanography*, *26*(2), 68–79.
Jaeger, G. S., & Mahadevan, A. (2018). Submesoscale-selective compensation of fronts in a salinity-stratified ocean. *Science Advances*, *4*(2), e1701504.
Jansen, R. W., Shen, C. Y., Chubb, S. R., Cooper, A. L., & Evans, T. E. (1998). Subsurface, surface, and radar modeling of a Gulf Stream current convergence. *Journal of Geophysical Research*, *103*(C9), 18,723–18,743. https://doi.org/10.1029/98JC01195
Johannessen, J. A., Kudryavtsev, V., Akimov, D., Eldevik, T., Winther, N. G., & Chapron, B. (2005). On radar imaging of current features: 2. Mesoscale eddy and current front detection. *Journal of Geophysical Research*, *110*, C07017. https://doi.org/10.1029/2004JC002802
Klein, P., & Lapeyre, G. (2009). The oceanic vertical pump induced by mesoscale and submesoscale turbulence. *Annual Review of Marine Science*, *1*, 351–375.
Kudryavtsev, V., Akimov, D., Johannessen, J., & Chapron, B. (2005). On radar imaging of current features: 1. Model and comparison with observations. *Journal of Geophysical Research*, *110*, C07016. https://doi.org/10.1029/2004JC002505
Kudryavtsev, V., Kozlov, I., Chapron, B., & Johannessen, J. A. (2014). Quad-polarization SAR features of ocean currents. *Journal of Geophysical Research: Oceans*, *119*, 6046–6065. https://doi.org/10.1002/2014JC010173
Kudryavtsev, V., Myasoedov, A., Chapron, B., Johannessen, J. A., & Collard, F. (2012a). Joint Sun-glitter and radar imagery of surface slicks. *Remote Sensing of Environment*, *120*, 123–132.
Kudryavtsev, V., Myasoedov, A., Chapron, B., Johannessen, J. A., & Collard, F. (2012b). Imaging mesoscale upper ocean dynamics using synthetic aperture radar and optical data. *Journal of Geophysical Research*, *117*, C04029. https://doi.org/10.1029/2011JC007492
Kudryavtsev, V., Yurovskaya, M., Chapron, B., Collard, F., & Donlon, C. (2017). Sun glitter imagery of surface waves. Part 2: Waves transformation on ocean currents. *Journal of Geophysical Research: Oceans*, *122*, 1384–1399. https://doi.org/10.1002/2016JC012426
Luketina, D. A., & Imberger, J. (1987). Characteristics of a surface buoyant jet. *Journal of Geophysical Research*, *92*(C5), 5435–5447.
Lund, B., Haus, B. K., Horstmann, J., Graber, H. C., Carrasco, R., Laxague, N. J. M., et al. (2018). Near-surface current mapping by ship-board marine X-band radar: A validation. *Journal of Atmospheric and Oceanic Technology*, *35*(5), 1077–1090.
Lyzenga, D. R. (1991). Interaction of short surface and electromagnetic waves with ocean fronts. *Journal of Geophysical Research (1978–2012)*, *96*(C6), 10,765–10,772.
Lyzenga, D. R. (1998). Effects of intermediate-scale waves on radar signatures of ocean fronts and internal waves. *Journal of Geophysical Research*, *103*(C9), 18,759–18,768.
Mahadevan, A. (2016). The impact of submesoscale physics on primary productivity of plankton. *Annual Review of Marine Science*, *8*(1), 161–184. PMID: 26394203 https://doi.org/10.1146/annurev-marine-010814-015912
Marmorino, G. O., Lyzenga, D. R., & Kaiser, J. A. C. (1999). Comparison of airborne synthetic aperture radar imagery with in situ surface-slope measurements across Gulf Stream slicks and a convergent front. *Journal of Geophysical Research*, *104*(C1), 1405–1422.
Marmorino, G. O., & Trump, C. (1994). A salinity front and current rip near Cape Hatteras, North Carolina. *Journal of Geophysical Research*, *99*(C4), 7627–7637.
Marmorino, G. O., & Trump, C. L. (1996). High-resolution measurements made across a tidal intrusion front. *Journal of Geophysical Research*, *101*(C11), 25,661–25,674.
Matthews, J. (2005). Stereo observation of lakes and coastal zones using aster imagery. *Remote sensing of environment*, *99*(1), 16–30.
Matthews, J. P., & Awaji, T. (2010). Synoptic mapping of internal-wave motions and surface currents near the Lombok Strait using the along-track stereo Sun glitter technique. *Remote Sensing of Environment*, *114*(8), 1765–1776.
Matthews, J. P., Ostrovsky, L., Yoshikawa, Y., Komori, S., & Tamura, H. (2017). Dynamics and early post-tsunami evolution of floating marine debris near Fukushima Daiichi. *Nature Geoscience*, *10*(8), 598.
Matthews, J. P., Wismann, V. R., Lwiza, K., Romeiser, R., Hennings, I., & De Loor, G. P. (1997). The observation of the surface roughness characteristics of the rhine plume frontal boundaries by simultaneous airborne thematic mapper and multifrequency helicopter-borne radar scatterometer. *International Journal of Remote Sensing*, *18*(9), 2021–2033.
Matthews, J. P., & Yoshikawa, Y. (2012). Synergistic surface current mapping by spaceborne stereo imaging and coastal HF radar. *Geophysical Research Letters*, *39*, L17606. https://doi.org/10.1029/2012GL052546
McClain, E. P., & Strong, A. E. (1969). On anomalous dark patches in satellite-viewed sunglint areas. *Monthly Weather Review*, *60*(65), 70.
McWilliams, J. C. (2016). Submesoscale currents in the ocean. *Proceedings of the Royal Society A: Mathematical, Physical and Engineering Sciences*, *472*(2189), 20160117.
Molinari, R., & Kirwan, A. D. Jr. (1975). Calculations of differential kinematic properties from lagrangian observations in the western Caribbean Sea. *Journal of Physical Oceanography*, *5*, 483–491.
Morrow, R., Fu, L.-L., Ardhuin, F., Benkiran, M., Chapron, B., Cosme, E., et al. (2019). Global observations of fine-scale ocean surface topography with the Surface Water and Ocean Topography (SWOT) mission. *Frontiers in Marine Science*, *6*, 232. https://doi.org/10.3389/fmars.2019.00232
Mouche, A., & Chapron, B. (2015). Global C-band Envisat, RADARSAT-2 and Sentinel-1 SAR measurements in copolarization and cross-polarization. *Journal of Geophysical Research: Oceans*, *120*, 7195–7207. https://doi.org/10.1002/2015JC011149
Mueller, J. L., & LaViolette, P. E. (1981). Color and temperature signatures of ocean fronts observed with the Nimbus-7 CZCS, *Oceanography from space* (pp. 295–302). Boston, MA: Springer US.
Munk, W., Armi, L., Fischer, K., & Zachariasen, F. (2000). Spirals on the sea. *Philosophical transactions of the Royal Society of London A*, *456*, 1217–1280.
Novelli, G., Guigand, C. M., Cousin, C., Ryan, E. H., Laxague, N. J. M., Dai, H., et al. (2017). A biodegradable surface drifter for ocean sampling on a massive scale. *Journal of Atmospheric and Oceanic Technology*, *34*(11), 2509–2532.

O'Donnell, J., Marmorino, G. O., & Trump, C. L. (2002). Convergence and downwelling at a river plume front. *Journal of Physical Oceanography*, *28*(7), 1481–1495.

Ohlmann, J. C., Molemaker, M. J., Baschek, B., Holt, B., Marmorino, G., & Smith, G. (2017). Drifter observations of submesoscale flow kinematics in the coastal ocean. *Geophysical Research Letters*, *44*, 330–337. https://doi.org/10.1002/2016GL071537

Okubo, A., Ebbesmeyer, C. C., & Helseth, J. M. (1976). Determination of Lagrangian deformations from analysis of current followers. *Journal of Physical Oceanography*, *6*, 524–527.

Özgökmen, T. M., Beron-Vera, F. J., Bogucki, D., Chen, S. S., Dawson, C., Dewar, W., et al. (2014). Research overview of the Consortium for Advanced Research on Transport of Hydrocarbon in the Environment (CARTHE). *International Oil Spill Conference Proceedings*, *2014*(1), 544–560. https://doi.org/10.7901/2169-3358-2014.1.544

Pearson, J., Fox-Kemper, B., Barkan, R., Choi, J., Bracco, A., & McWilliams, J. C. (2019). Impacts of convergence on structure functions from surface drifters in the Gulf of Mexico. *Journal of Physical Oceanography*, *49*(3), 675–690.

Phillips, O. M. (1984). On the response of short ocean wave components at a fixed wavenumber to ocean current variations. *Journal of Physical Oceanography*, *14*, 1425–1433.

Rascle, N., Chapron, B., Ponte, A., Ardhuin, F., & Klein, P. (2014). Surface roughness imaging of currents shows divergence and strain in the wind direction. *Journal Of Physical Oceanography*, *44*(8), 2153–2163.

Rascle, N., Molemaker, J., Marié, L., Nouguier, F., Chapron, B., Lund, B., & Mouche, A. (2017). Intense deformation field at oceanic front inferred from directional sea surface roughness observations. *Geophysical Research Letters*, *44*, 5599–5608. https://doi.org/10.1002/2017GL073473

Rascle, N., Nouguier, F., Chapron, B., Mouche, A., & Ponte, A. (2016). Surface roughness changes by finescale current gradients: Properties at multiple azimuth view angles. *Journal of Physical Oceanography*, *46*(12), 3681–3694.

Rascle, N., Nouguier, F., Chapron, B., & Ocampo-Torres, F. J. (2018). Sunglint images of current gradients at high resolution: Critical angle and directional observing strategy. *Remote Sensing of Environment*, *216*, 786–797.

Rodríguez, E., Wineteer, A., Perkovic-Martin, D., Gál, T., Stiles, B. W., Niamsuwan, N., & Monje, R. R. (2018). Estimating ocean vector winds and currents using a Ka-band pencil-beam Doppler scatterometer. *Remote Sensing*, *10*(4), 576.

Shcherbina, A. Y., D'Asaro, E. A., Lee, C. M., Klymak, J. M., Molemaker, M. J., & McWilliams, J. C. (2013). Statistics of vertical vorticity, divergence, and strain in a developed submesoscale turbulence field. *Geophysical Research Letters*, *40*, 4706–4711. https://doi.org/10.1002/grl.50919

Simpson, J. H. (1981). The shelf-sea fronts: Implications of their existence and behaviour. *Philosophical Transactions of the Royal Society of London. Series A, Mathematical and Physical Sciences*, *302*(1472), 531–546.

Simpson, J. E., & Britter, R. E. (1979). The dynamics of the head of a gravity current advancing over a horizontal surface. *Journal of Fluid Mechanics*, *94*(3), 477–495.

Thompson, D. R., & Gasparovic, R. F. (1986). Intensity modulation in SAR images of internal waves. *Nature*, *320*, 345–348.

Torres, R., Snoeij, P., Geudtner, D., Bibby, D., Davidson, M., Attema, E., et al. (2012). GMES Sentinel-1 mission. *Remote Sensing of Environment*, *120*, 9–24. https://doi.org/10.1016/j.rse.2011.05.028

Woodson, C. B., & Litvin, S. Y. (2015). Ocean fronts drive marine fishery production and biogeochemical cycling. *Proceedings of the National Academy of Sciences*, *112*(6), 1710–1715.

Zhong, Y., Bracco, A., & Villareal, T. A. (2012). Pattern formation at the ocean surface: Sargassum distribution and the role of the eddy field. *Limnology and Oceanography: Fluids and Environments*, *2*(1), 12–27.